A Front Tracking Method for Simulation of Interfacial Flows with Soluble Surfactants

by

Emrah Gölbaşı

A Thesis Submitted to the

Graduate School of Engineering

in Partial Fulfillment of the Requirements for

the Degree of

Master of Science

in

Mechanical Engineering

Koç University

September, 2006

Koç University

Graduate School of Sciences and Engineering

This is to certify that I have examined this copy of a master's thesis by

Emrah Gölbaşı

and have found that it is complete and satisfactory in all respects,
and that any and all revisions required by the final
examining committee have been made.

Committee Members:

_____
Assistant Prof. Metin Muradoğlu (Advisor)

_____
Assistant Prof. Murat Sözer

_____
Assistant Prof. Esra Sorgüven

Date: _____

To my family

ABSTRACT

Surfactants are chemical substances that can accumulate on interfaces and lower the interfacial tension. The accumulation of surfactant at the interface between two fluids may significantly alter the dynamics of a multiphase flow. Nonuniform distribution of surfactant can cause large variations on the mechanical response of the system and leads to the nonuniform distribution of capillary (normal) and Marangoni (tangential) stresses which can significantly affect the deformation of drops and even may result in breakup. In this thesis, a finite-difference/front tracking method is developed for computations of interfacial flows with soluble surfactants to understand the effects of surfactants on a strongly deforming interface. Surfactant transport equations of the bulk and interface surfactant concentrations are solved together with the incompressible Navier-Stokes equations. A nonlinear equation of state is used to relate the interfacial tension to surfactant concentration at the interface. In order to validate the numerical algorithm, several simple test cases are considered and the numerical results are found to be in a good agreement with the analytical solutions. The method is then applied to the cleavage of a droplet by surfactant - a problem proposed by Greenspan (1977,1978) as a model for cytokinesis of biological cells.

Keywords: Soluble surfactant, front-tracking method, droplet cleavage.

ÖZET

Yüzey aktif maddeler, çok fazlı akışkan sistemlerinin ortak yüzeylerinde birikebilme ve yüzey gerilimini düşürebilme özelliğine sahip kimyasallardır. Yüzey aktif maddelerin iki karışmaz sıvının arayüzeyinde birikmesi, çok fazlı akışların dinamiğini önemli ölçüde etkiler. Yüzey aktif maddelerin arayüzeyler üzerindeki homojen olmayan dağılımları ise akış sistemlerinin mekanik tepkileri üzerinde büyük etkilere yol açar. Buna ilave olarak yüzey aktif maddeler, normal (kapiler) ve teğetsel (Marangoni) yöndeki kuvvetlerin dağılımını değiştirerek damlaların deformasyonlarını ve bölünmelerini önemli ölçüde etkiler. Bu çalışmada, yüzey aktif maddelerin deforme olan yüzeyler üzerindeki etkisini anlamak amacı ile, çözünür yüzey aktif madde içeren çok fazlı akışların hesaplanmasında kullanılmak üzere Sonlu Farklar/Arayüz izleme metodu geliştirildi. Arayüzde ve damlanın dışındaki fazda yüzey aktif madde taşınım denklemleri, sıkıştırılamaz Navier-Stokes denklemleri ile beraber çözüldü. Yüzey gerilimini yüzey aktif maddenin fonksiyonu olarak tanımlamak için, lineer olmayan bir durum denklemi kullanıldı. Nümerik algoritma basit test problemlerine uygulandı ve nümerik sonuçların analitik sonuçlar ile uyuştuğu gözlendi. Daha sonra, geliştirilen metod H. P. Greenspan (1977, 1978) tarafından biyolojik hücre bölünmesi modeli olarak önerilen *yüzey aktif madde etkisinde damla bölünmesi* problemine başarı ile uygulandı.

Anahtar kelimeler: Çözünür yüzey aktif madde, arayüz izleme metodu, damla bölünmesi.

ACKNOWLEDGMENTS

First, I would like to thank my thesis advisor Dr. Metin Muradoğlu for his great supervision and continuous support. He shared his knowledge and experience with me, paid attention to all the steps of my thesis, and provided me his recommendations that guided me.

I thank Dr. Murat Sözer and Dr. Esra Sorgüven for their readings, comments for my thesis and for being in my thesis committee.

Many thanks are due to my grad student friends, especially Satayef and Soner, whose friendship have made the years in Koç University a memorable time in my life. Also, I would like to thank my former research group friend Murat Bahadır Soydan for his friendly help at the first year of my graduate study.

All this would not be possible without the support of my family; my mother Aslı Gölbaşı, my father Yalçın Gölbaşı, and my uncle Vedat Gölbaşı. I would like to thank them for their never ending and unconditional love.

Finally, I would like to thank my girlfriend, Özlem, for her invaluable support, patience, encouragement, and love.

TABLE OF CONTENTS

LIST OF TABLES

LIST OF FIGURES

xi

NOMENCLATURE

FD/FT   Finite difference / Front Tracking

ENO   Essentially non-oscillatory

r and z radial and axial coordinates

u_r radial velocity

u_z axial velocity

p pressure

ρ_o density of the ambient fluid

ρ_d density of the drop

μ_o viscosity of the ambient fluid

μ_d viscosity of the drop

t physical time

t^* dimensionless time

s arc length

R radius of the tube

σ surface tension

κ curvature

$\mathbf{x}$ location of a front point

$\mathbf{x}_f$ location of the front

$\mathbf{n}$ surface normal vector

$\mathbf{i_r}$ radial component of surface normal vector

$\mathbf{i_z}$ axial component of surface normal vector

δ Delta function

d drop diameter

a initial drop radius

Γ surfactant concentration at the interface

Γ_∞ maximum surfactant concentration at the interface

D_s surface diffusion coefficient

D_c bulk diffusion coefficient

C bulk surfactant concentration

C_∞ bulk surfactant concentration far from the interface

σ_s surface tension of a clean interface

$\mathcal{L}$ length scale

$\mathcal{V}$ velocity scale

$\mathcal{T}$ time scale

Re Reynolds number

Pe_c bulk Peclet number

Pe_s surface Peclet number

Bi Biot number

Da Damkohler number

E elasticity number

k adsorption number

Ω bandwidth for introducing the bulk surfactant

Chapter 1

INTRODUCTION

1.1 Motivations

The term surfactant, which is derived from the words surface active agent, is of fundamental importance in many industrial and biomedical applications involving multiphase flows. Throughout the history, surfactants have played an important role in many practical applications including detergents, emulsifiers, paints and adhesives [3]. In some situations, their presence can have positive effects on the process, while in other situations they are not desired but it is difficult to remove them from the system. Surfactants are extensively used as excipients in drug delivery [4], emulsification [5], ceramic processing [6], petroleum and oil recovery [7], coating, wetting [8] and in many other processes. As its name indicates, surfactants are active on interfaces that seperate two immiscible fluids. The tendency to accumulate at the interfaces, lowering the interfacial tension and solubility in liquids are the common properties of surfactants.

Structurally, a surfactant molecule consists of a hydrophobic tail which is generally soluble in oil but insoluble in water and hydrophilic (or polar) head which is generally insoluble in oil and soluble in water. Sodium dodecyl sulfate ($CH_3(CH_2)_{11}OSO_3Na$), cetrimonium bromide ($C_{19}H_{42}BrN$) and cetyl alcohol ($CH_3(CH_2)_{15}OH$) are typical examples for the different types of surfactant molecules [3]. Figure 1.1 illustrates a schematic of a typical surfactant molecule [7]. The adsorption characteristics of a surfactant molecule stem from the existence of two groups in its structure and depend on the properties of the surfaces that the surfactant affect. Surfactant molecules at the interface can be positioned in two ways due to the solubility of the surfactant. As sketched in Fig. 1.2a, when a surfactant is soluble in phase 1, i.e., in bulk phase, the hydrophilic head is outside the drop. On the contrary, if phase 1 and phase 2 interchange, the hydrophilic head is inside the drop because of its

solubility in phase 1 which is illustrated in Fig. 1.2b. In this thesis, the system consists of two immiscible liquids and surfactant is soluble in bulk phase, so that the surfactant molecules stick on the surface by the hydrophilic head positioned at the outside the drop.
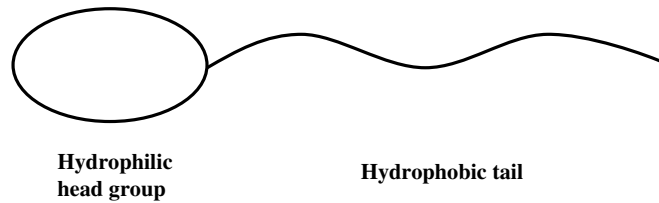
Figure 1.1: Schematic illustration of a surfactant molecule.
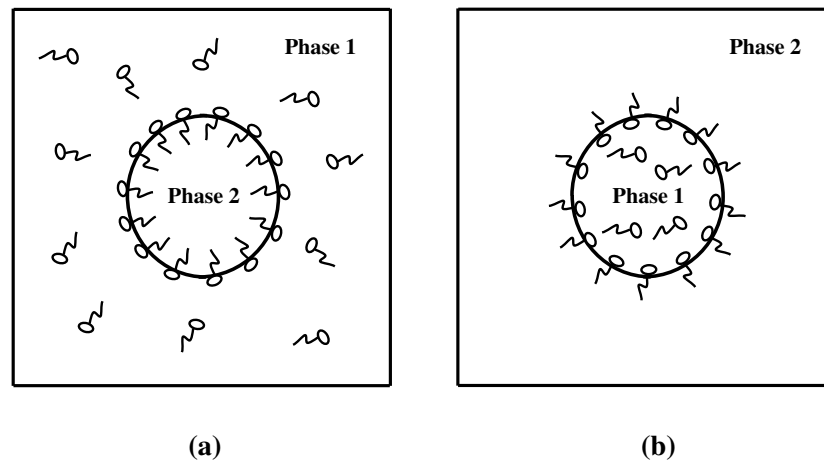
Figure 1.2: Schematic illustration of the positioning of surfactant molecules on the drop interface. Surfactant is soluble in phase 1.

The accumulation process at interfaces is provided by the adsorption of surfactant. Lowering the free energy of the phase boundary, which the surfactant accumulate on, is the driving force for the adsorption. The interfacial free energy is the amount of work required to expand the interface and interfacial tension is defined as the interfacial free energy per unit area. As the interface is covered by the surfactant molecules, interfacial tension decreases and less work is required to expand the interface.

Appearently, there is an upper bound for the interfacial tension lowering effect of the surfactants. When this limit is reached, surfactant is no more soluble in the liquid phase and micelles start to form in the bulk solution. Table 1.1 illustrates some typical values of surface and interfacial tension of liquid/liquid and liquid/gas systems. In some specialized systems, interfacial tension can be lowered drastically, from 1-10 mN/m to the values in the range of 10^{-3} mN/m or below. For instance, such systems are of interest for enhanced oil recovery [1]. The amount of interfacial tension decrease depends on the surfactant concentration at the interface. Nonuniform distribution of the surfactant at the interface causes nonuniform distribution of surface tension and surface forces which can affect the motion and the deformation of drops and bubbles [9, 10, 11, 12]. These basic but vital properties of surfactants lead to a clear understanding of solubility and transport mechanism of surfactants in different systems.

To summarize, surfactants are among the most widely used groups of chemicals in the world not only because they are extremely important in conventional process industry, but also because they find increasingly useful applications in such diverse fields as microelectronics, microfluidics and biotechnology. In addition, surfactants are also used to model division of biological cells [10]. Although the surfactants have been studied extensively for many years, it is still a challenging task to model the effects of surfactants on the interfacial flows due to strongly nonlinear complex interactions between the fluids and deforming interfaces, finite rate of mass transfer along the interface as well as between the bulk fluids and the interface.

Air-Water	$72 - 73$
Air-aqueous surfactant solution	$28 - 30$
Aliphatic hydrocarbon-water	$40 - 50$
Aromatic hydrocarbon-water	$20 - 30$
Hydrocarbon-aqueous surfactant solution	$1 - 10$

Table 1.1: Typical values of surface and interfacial tensions(mN/m) [1].

1.2   Literature Review

Deposition of a surface active material on a viscous droplet and the effect of various surface tension on its shape has been a long term interest of researchers from both biological and mechanical point of view. In the context of the present study, experimental works for the deformation of a droplet under the effect of surfactant arise from the fluid mechanical simulation studies of cell cleavage or cytokinesis, i.e., the division of a biological mother cell into two daughter cells including a series of repetitous shape changes [13]. Many experimental studies are based on the local surface tension changes of an oil drop, which is a simple model of a biological cell. McClendon and Spek (1918) showed that an oil droplet can be divided into two by manipulating its surface tension with the effect of a surfactant - an alkali or detergent (see review by Rappaport [14]). Greenspan [10] proposed a specific simulation for cell cleavage by studying the deformation of a droplet under the influence of surfactant. He repeated Spek's experiment with updated materials and demonstrated that the oil droplet passed through a series of large deformations, even it goes into a whole breakup under the effect of the surfactants. The final shape of the oil droplet was very analogous to the one in the cytokinesis [14]. The experimental procedure was to apply a symmetric continuous flow of surfactant by syringes to the poles of the oil droplet neutrally buoyant in the surrounding solvent. As the surfactant deposited on the interface, surface tension gradients occured and this caused the droplet contracted from the equator. Moreover, if the surfactant deposition was in short bursts, droplet deformed at the beginning but recovered its spherical shape very quickly. Figure 1.3 represents a schematic representation of the experiment which is going to be explained in detail in Section 4.1.1.

Greenspan's hydrodynamic theory of cell division was mainly based on the unstable contractions of surface towards equator stemmed from the equatorial and polar tension difference. The relative differential of surface tension is due to the chemical activity of the tension elements, namely the polymerization or depolymerization of microfilaments attached to the cell membrane. By the change of element concentration, surface tension increases at the poles or decreases at the equator which causes developing the surface tension gradients producing a surface flow from poles to equator and contractile forces become dominant which may lead to cleavage. This unstable mechanical process tends to continue indefinitely after it starts. Greenspan also conducted some theoritical studies by using perturbation techniques
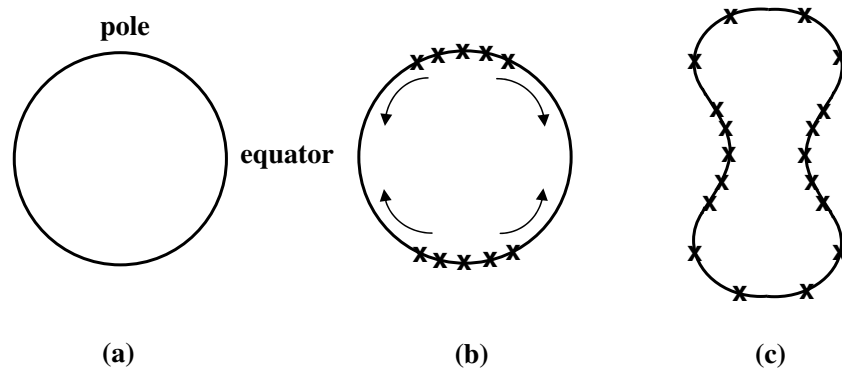
Figure 1.3: Schematic illustration of the Greenspan's oil droplet experiment. (a) no surfactant at the interface at the initial state of the drop. (b) Surfactant applied on the drop poles simultaneously. (c) Surface tension gradients occur due to the nonuniform distribution of the surfactant and oil drop contracts towards the equator.

to support the model he proposed [11]. The model assumes that the drop is axisymmetric with surfactant released from the poles. However, he could only describe the initial stages of the droplet deformation and the theory was unable to explain the large deformations.

Sapir and Nir [15] tried to explain the entire deformation of the oil droplet in Greenspan's experiment. In their treatment, the governing equations was assumed to be Stokes equations where the boundary condition was described by the balance of viscous forces and surface tension forces. The moving boundary problem was solved by using boundary integral method. A transport equation for surfactant was also included in the model. Although they tested a large number of surface tension distributions, they were unable to achieve the large deformations observed in Greenspan's experiment. The largest deformation was attained when there is no change in the surface tension distribution during the entire deformation and it was only 20% of the initial neck radius.

Zinemanas and Nir [16] presented a fluid mechanical simulation of cytokinetic cell deformation by combining the equations of motion with concentration and distribution balances for active contractile microfilaments on the cell surface. The contribution of the latter condition is the same as the activity of surfactant on a viscous droplet where it provides a dynamical evolution of surface forces and deformation by introducing an anisotropic surface

tension.

He and Dembo [17] presented numerical computations of Greenspan's experiment by using a finite element method, tried to understand the physical reasons for the failure of Sapir-Nir theory and proposed some modifications. They defined a special case of surface tension distribution as a function of axial distance and achieved a nonuniform distribution of pressure. Although they tested the model in a wide range of surfactant distributions, their theory could not account for the cleavage of a droplet observed by Greenspan. They concluded that the pure action of surface tension was not sufficient to make a droplet undergo a complete cleavage or large deformations. In order to explain the deep furrowing of a droplet under the effect of surfactant, they proposed a traction force, namely phoretic force, which can be regarded as the integrated result of a tangential traction that acts in a thin interfacial layer seperating the particle from the bulk phase. They assumed that this transport effect originated force is proportional to the surface tension gradient and has an opposite sign. They achieved large deformations by introducing the phoretic force to their model but they stated that this cannot be an explanation for Greenspan's theory because of the high viscosity of the bulk fluid unlike the oil droplet experiment.

More recently, He and Dembo [18] described a continuum model of the sea urchin egg during the first cleavage division and extended the standart model of Greenspan [10, 11] and Sapir and Nir [15]. They proposed that the sea urchin egg is mechanically equivalent to a small droplet of passive watery fluid and its cytoplasmic material consists of two isotropic materials, i.e., network and solvent phases. They solved the mass and momentum conservation equations for both phases by using Galarkin finite element method. They included their model the reaction and hydrodynamic friction between the network and solvent phases as well as the attractive and repulsive stresses due to the activity of cellular filaments.

Researches on dynamical effects of interfacial tension gradients caused by surfactants are not only stemmed from the fluid mechanical simulation of cell division and cell mechanics. There have been many previous studies concerned with the effect of surfactants on drops and bubbles in extensional flows. Stone and Leal [12] examined the effects of insoluble surfactants on drop deformation and breakup in extensional flows at low Reynolds numbers. They described a numerical procedure based upon the boundary integral method which

can analyse the time dependent convective/diffusion equation for surfactant transport on the interface. They showed that the deformation is influenced by the accumulation of surfactant at the ends of the drop due to the convective effect of the external flow and dilution of the surfactant concentration due to the expanding surface of the deformed drop. Milliken et al. [19] extended their work for different drop and suspending fluid viscosities, unsteady drop motions and nonlinear equation of state. They found that the effect of surfactant decreases by the increasing viscosity ratio. Moreover, for small viscosity ratios and convection dominated motion, they observed spindlelike pointed shapes which lead to tip streaming observed experimentally. Pawar and Stebe [20] examined the effects of insoluble surfactants on drop deformation in extensional flows. They found that the linear equation of state, which relates the surface tension with surfactant distribution, is not valid for moderate surfactant concentrations and took into consideration the surface saturation and molecular interactions of surfactant. Eggleton and Stebe [21] accounted for surfactant mass transfer with the bulk in the problem of initially spherical droplet deforming in an extensional flow. They showed that the drop behaviour is seriously affected by the surfactant mass transfer rate and the concentration of surfactant at the interface. Eggleton et al. [22] investigated the effects of surfactant on the tip-streaming occuring in a linear extensional flow. They found that as the surfactant is swept towards the drop poles, surface tension approaches to zero at the poles and sharp gradients in surface tension lead to the emission of a thread where it can result with the seperation of small droplets from the tail part, i.e., tip streaming. This results are consistent with the studies of Stone and Leal [12].

Moreover there have been many studies examining the effects of surfactants on the motion of drops and bubbles in a tube. He et al. [23] studied the influence of surfactants on the pressure-driven motion of a buoyant drop in a tube. They focused on the adsorption effect and confirmed the retarding effect of surfactant on the drop motion. Borhan and Mao [24] studied the drop translation in a straight capillary tube including the effects of insoluble surfactants. They observed a reentrant cavity at the back of the drop which extends as the surfactant convection becomes stronger. Same results are confirmed by Tsai and Miksis [25]. Surfactant concentrations was very low in the studies of Borhan and Mao and of Tsai and Miksis where they used a linear surface equation of state. Johnson and Borhan [26] extended their work by using a nonlinear equation of state. They examined the

drop behaviour at high surfactant concentrations and accounted for the physical chemistry of the insoluble surfactants. They found that for strong cohesive interactions, drop mobility increases with the increasing surfactant coverage. More recently, Johnson and Borhan [27] studied the effects of bulk-soluble surfactans on the dynamics of a drop translating through a cylindirical capillary tube at low-Reynolds numbers by using boundary integral method.

Computational studies on drop behaviour under the influence of surfactants are not only restricted with the Stokes flow based on the boundary integral methods, but there are also several studies using full Navier-Stokes models. Drumright-Clarke and Renardy [28] considered the effects of insoluble surfactants on the deformation of a three-dimensional viscous drop, breakup and drop size distribution of daughter droplets in shear flow where the viscosity and the density of the drop are equal to the suspending fluid. They developed a volume-of-fluid method by using a linear equation of state. Lee and Pozrikidis [29] investigated the effects of insoluble surfactants on the deformation of and the structure of flow around a drop in two dimensional channels. Their methodology combines the Peskin's immersed interface method, diffuse-interface approximation and a finite-volume method for integrating the convection-diffusion equation of surfactant at the interface. Xu and Zhao [30] presented a level-set method to simulate surfactant transport on a deformable interface without coupling the method to a flow solver. Xu et al. [31] extended their work by integrating the method to a flow solver. James and Lowengrub [32] proposed a surfactant-conserving volume-of-fluid method to examine the insoluble surfactant effect on interfacial flows. Olgac and Muradoglu [33] recently studied the effects of soluble surfactants on the motion and breakup of viscous drops in straight and constricted capillaries by using a Finite Volume/Front-Tracking method where the bulk surfactant concentration is assumed to remain constant throughout the process.

1.3   Contributions Made in this Work

A general computational procedure is developed here based on the finite-difference/front-tracking (FD/FT) method [34] for simulations of interfacial flows with soluble surfactants. The governing equations for axisymmetric geometry are solved numerically on a fixed, regular, staggered grid where the drop interface is represented by a Lagrangian grid with connected marker points. Convection/diffusion equations for surfactant at the interface

and in the bulk are solved fully coupled with the flow equations. Nonlinear equation of state is taken into account to relate the surface tension to surfactant concentration at the interface. First, the numerical algorithm is validated for some simple test cases where the analytical solutions are available. Then, in order to understand the effects of surfactant on the deformation and breakup mechanism of drops and bubbles, the method is applied to the cleavage of a viscous droplet which is proposed as a cell division model by Greenspan [10, 11]. The main advantage of the present method is that it can describe the large deformations and breakup of droplets along with the accurate treatment of the surface tension and bulk solubility. Simulations with a wide range of parameters are presented and the conditions for drop cleavage are discussed.

<div align="center">

Chapter 2

FORMULATION AND NUMERICAL METHOD

</div>

The numerical technique used in this study is based on the finite-difference/front tracking method developed by Unverdi and Tryggvason [34]. An axisymmetric version of the method is used in simulations in order to treat the physical problem accurately while keeping the computation time manageable. This chapter begins with the presentation of the governing equations that describe the behaviour of a viscous droplet under the influence of surfactant. The surfactant is assumed to be soluble in bulk phase and transported to the interface by an adsorption-desorption mechanism. Then the governing equations are nondimensionalized and the governing nondimensional numbers are identified. After that the numerical technique is described in detail and then the overall solution procedure is summarized. Finally treatment of the drop breakup is explained.

2.1 Governing Equations

The computational domain and the physical problem are illustrated in Fig. 2.1. The domain is axisymmetric with the left boundary being the axis of symmetry. The drop is initially spherical and has the diameter d. Two phases are seperated by an interface with various surfactant concentrations. There is a soluble surfactant at the bulk phase that is transported onto the interface. The radius of the tube is R and the length of the tube is unrestricted but the computational domain extends $3R$ in the axial direction for computational convenience. Arc length is measured in clockwise direction from the top of the drop. The origin of the cylindirical coordinates is set at the bottom-left corner of the domain and is on the axis of symmetry. The motion of continuous and dispersed phases is governed by incompressible Navier-Stokes equations and is solved everywhere, both inside and outside the drop. As discussed by Unverdi and Tryggvason [34], a single set of conservation equations for the entire flow field can be written as long as the density, viscosity and molecular diffusion coefficient jumps across the interface are accounted for and surface tension is included.
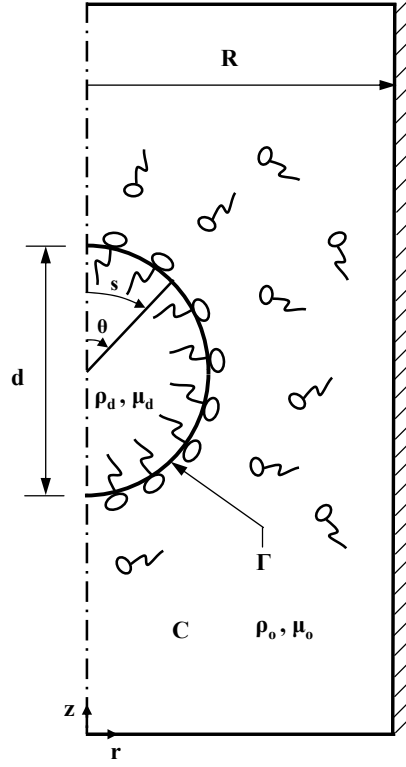
Figure 2.1: A schematic diagram of the computational domain with surfactant at the interface and soluble at the bulk.

In cylindirical coordinates, time dependent Navier-Stokes equations in axisymmetric geometry can be written in the conservative form as

$$\frac{\partial}{\partial t}(\rho r u_r) + \frac{\partial}{\partial r}(\rho r u_r u_r) + \frac{\partial}{\partial z}(\rho r u_z u_r) = -r\frac{\partial p}{\partial r} + r\frac{\partial}{\partial r}(2\mu\frac{\partial u_r}{\partial r}) + 2\mu r\frac{\partial u_r}{\partial r} +$$
$$\frac{\partial}{\partial z}[\mu r(\frac{\partial u_z}{\partial r} + \frac{\partial u_r}{\partial z})] + \int_A \sigma(\Gamma)\kappa\mathbf{n}\delta(\mathbf{x} - \mathbf{x_f}) \cdot \mathbf{i_r}dA, \qquad (2.1)$$

$$\frac{\partial}{\partial t}(\rho r u_z) + \frac{\partial}{\partial r}(\rho r u_r u_z) + \frac{\partial}{\partial z}(\rho r u_z u_z) = -r\frac{\partial p}{\partial z} + \frac{\partial}{\partial r}[\mu r(\frac{\partial u_z}{\partial r} + \frac{\partial u_r}{\partial z})] +$$
$$\frac{\partial}{\partial z}(2\mu r\frac{\partial u_z}{\partial z}) + \int_A \sigma(\Gamma)\kappa\mathbf{n}\delta(\mathbf{x} - \mathbf{x_f}) \cdot \mathbf{i_z}dA, \qquad (2.2)$$

where u_r and u_z are the radial and axial velocities, p is the pressure and ρ and μ are the discontinuous density and viscosity fields, respectively. In Eq.(2.1) and (2.2), the contribution

of the surface tension is included as a body force. Here, σ is the surface tension that is the function of surfactant concentration Γ at the interface, κ is the twice of the mean curvature, $\mathbf{n}$ is the unit normal vector to the interface seperating two phases, $\mathbf{i_r}$ and $\mathbf{i_z}$ are the radial and axial components of a surface normal vector, A is the surface area of the interface and dA denotes the surface area element of the interface, respectively. δ is the three dimensional delta function describing that the surface tension is concentrated at the boundary between two fluids, where $\mathbf{x}$ is the location of a point where the function is evaluated and $\mathbf{x_f}$ is the location of the front.

Both fluids are incompressible and the density remains constant following a fluid particle. Moreover fluids are immiscible so the viscosities of both fluids remain constant as well. Under these conditions, the denstiy and viscosity evolve by

$$\frac{D\rho}{Dt} = 0, \quad \frac{D\mu}{Dt} = 0, \tag{2.3}$$

where the material derivative is defined as $\frac{D()}{Dt} = \frac{\partial}{\partial t} + \mathbf{u} \cdot \nabla()$. Equation (2.3) is not solved directly and the material properties are set based on the indicator function as described in detail in Section 2.3. Using Eq. (2.3), the mass conservation equation reduces to the incompressibility condition given by

$$\frac{\partial}{\partial r}(r u_r) + \frac{\partial}{\partial z}(r u_z) = 0. \tag{2.4}$$

For a viscous droplet, surfactant effects are important. In order to examine the drop behaviour under the effect of surfactant, momentum equations are coupled with the surfactant transport equation at the interface and bulk surfactant evolution equation assuming that the surfactant is soluble at the bulk phase. Mass transfer between the bulk and interface is represented by a dynamic adsorption-desorption mechanism. Concentration of surfactant at the interface is defined as

$$\Gamma = \frac{M_s}{A}, \tag{2.5}$$

where M_s is the total mass of surfactant and A is the surface area of the drop.

The coupling of the momentum equations and surfactant transport equations is achieved through the surface tension term, i.e., the fifth term on the right hand side of Eq. (2.1) and the fourth term on the right hand side of Eq. (2.2). Surface tension is directly related to the surfactant concentration which lowers the surface tension nonlinearly. Their relationship is

determined by an equation of state derived from Langmuir adsorption [27], and must be specified before the convection/diffusion equation for surfactant is solved. In this model, surface tension is related to the surfactant concentration at the interface as

$$\sigma = \sigma_s + \mathcal{R}T\Gamma_\infty[\ln(1 - \frac{\Gamma}{\Gamma_\infty})], \tag{2.6}$$

where σ_s corresponds to the surface tension of a clean interface, $\mathcal{R}$ is the ideal gas constant, T is the absolute temperature and Γ_∞ is the maximum surface concentration for mono-layer adsorption. In particular, Γ_∞ is a theoritical limit which cannot be reached because surfactants have a limited area per molecule [21].

More complicated equations of state such as Frumkin equation state have also been used [20]. A major disadvantage of all equations of state used in the literature is that they predict physically unrealistic negative values for the surface tension when the surfactant concentration at the interface Γ approaches its maximum limit Γ_∞. As it can be seen in Eq. (2.6), surfactant concentration dependent surface tension is limited from above by the surface tension of a clean interface σ_s. In order to avoid the unphysical negative surface tension values, surface tension is limited below by a constant value as

$$\sigma = \max\left(\sigma_{min}, \sigma_s + \mathcal{R}T\Gamma_\infty[\ln(1 - \frac{\Gamma}{\Gamma_\infty})]\right), \tag{2.7}$$

where σ_{min} is the minimum surface tension and is given by $\sigma_{min} = \epsilon\sigma_s$ with ϵ being an arbitrary constant taken as 0.05 in the present computations.

Along the interface, surfactant concentration is governed by a convection/diffusion equation [35] given by

$$\frac{\partial\Gamma}{\partial t} + \nabla_s \cdot (\Gamma\mathbf{U_s}) = D_s\nabla_s^2\Gamma + \dot{S}_\Gamma, \tag{2.8}$$

where ∇_s denotes the surface gradient, $\mathbf{U_s}$ is the tangential velocity on the interface, D_s is the surface diffusivity and $\dot{S}_\Gamma$ is the source term. Note that the surface gradient operator is defined as

$$\nabla_s = \nabla - \nabla_n, \quad \nabla_n = \mathbf{n}(\mathbf{n} \cdot \nabla). \tag{2.9}$$

The flux from bulk to interface is both diffusion and adsorption-desorption controlled. Surfactant accumulated on a monolayer at the interface and source term in Eq. (2.8) is defined as

$$\dot{S}_\Gamma = \beta C_s(\Gamma_\infty - \Gamma) - \alpha\Gamma, \tag{2.10}$$

where β and α are the kinetic constants for adsorption and desorption, respectively. C_s denotes the concentration of surfactant in the fluid immediately adjacent to the interface. The bulk surfactant concentration C is governed by the convection/diffusion equation, i.e.,

$$\frac{\partial C}{\partial t} + \nabla \cdot (C\mathbf{U}) = \nabla \cdot (D_{co}\nabla C), \tag{2.11}$$

where D_{co} is a coefficient related to the bulk diffusion coefficient by scaling with indicator function I as

$$D_{co} = D_c(1 - I(r, z, t)). \tag{2.12}$$

The source term in Eq. (2.8) is related to the bulk concentration as [21]

$$\dot{S}_\Gamma = D_{co}(\mathbf{n} \cdot \nabla C \mid_s), \tag{2.13}$$

where the concentration gradient is evaluated at the interface. In the present method, the boundary condition at the interface given by Eq. (2.13) is first converted into a source term in a conservative manner by using a methodology that is consistent with the immersed boundary method [36]. We assume that there is a thin *adsorption layer* adjacent to the interface where all the mass transfer between the bulk and interface occurs. Figure 2.2 illustrates the schematic of the adsorption layer. By defining this transitional area, total amount of surfactant adsorped onto the interface is conserved. First, surfactant is adsorped onto the interface, then distributed over the adsorption layer and added to the bulk concentration evolution equation as a source term. Thus, Eq. (2.11) becomes

$$\frac{\partial C}{\partial t} + \nabla \cdot (C\mathbf{U}) = \nabla \cdot (D_{co}\nabla C) + \dot{S}_C, \tag{2.14}$$

where the source term for bulk concentration is defined as

$$\dot{S}_C = -\frac{\int_{interface} \dot{S}_\Gamma dA}{\int_{adsorptionlayer} dV}. \tag{2.15}$$

In Eq. (2.15), A and V are the interfacial surface area and the volume of the adsorption layer, respectively. By treating the problem in this manner, all the surfactant to be transferred to the interface is first consumed by the adsorption layer before the interface so the boundary condition at the interface simplifies to be $\mathbf{n} \cdot \nabla C \mid_s = 0$, which is automatically imposed by Eq. (2.12).
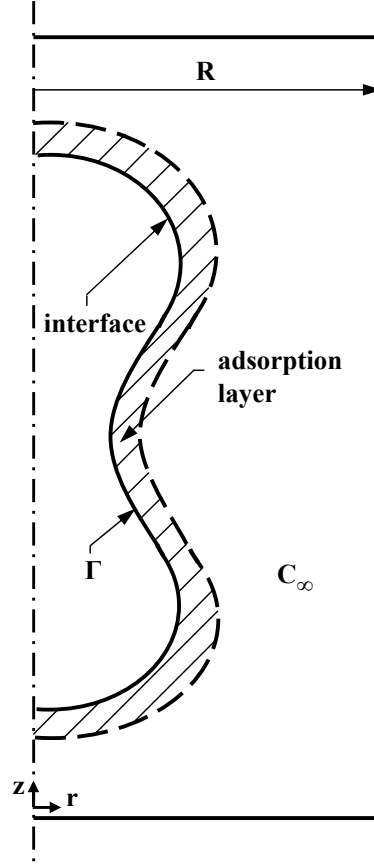
Figure 2.2: Schematic illustration of the adsorption layer.

2.2   Nondimensionalization of the Governing Equations

The governing equations are written in a nondimensional form to reduce the number of parameters and to render the problem in a compact form to analyse. The scaling parameters are defined as follows [19],

$$\mathcal{L} = a, \quad \mathcal{V} = \frac{\sigma_s}{\mu}, \quad \mathcal{T} = \frac{\mu a}{\sigma_s}, \tag{2.16}$$

where $\mathcal{L}$, $\mathcal{V}$ and $\mathcal{T}$ are the length, velocity and time scales, respectively. Then the continuity and momentum equations in a nondimensional form can be written as

$$\nabla^* \cdot \mathbf{u}^* = 0, \tag{2.17}$$

$$\frac{\partial \mathbf{u}^*}{\partial t^*} + \nabla^* \cdot (\mathbf{u}^* \mathbf{u}^*) = -\nabla^* p^* + \frac{1}{Re} \nabla^{*2} \mathbf{u}^* + f_s^*, \tag{2.18}$$

where $\mathbf{u}^*$ is the nondimensional velocity given by $\mathbf{u}^* = \{u_r^*, u_z^*\}^T$, f_s^* is the nondimensional body force and Re represents the Reynolds number defined as

$$Re = \frac{\rho_o \mathcal{V} \mathcal{L}}{\mu_o}. \tag{2.19}$$

Surfactant concentration at the interface Γ and bulk surfactant concentration C are nondimensionalized by the maximum surfactant concentration at the interface Γ_∞ and the surfactant concentration in the bulk fluid far from the interface C_∞, respectively.

Evolution equation for surfactant at the interface can be written in the nondimensional form as follows

$$\frac{\partial \Gamma^*}{\partial t^*} + \nabla_s^* \cdot (\Gamma^* \mathbf{U_s^*}) = \frac{1}{Pe_s} \nabla_s^{*2} \Gamma^* + Bi[C_s^*(k - k\Gamma^*) - \Gamma^*], \tag{2.20}$$

where Pe_s, Bi and k are the surface Peclet number, the Biot number and the adsorption number, respectively, defined as

$$Pe_s = \frac{\mathcal{V} \mathcal{L}}{D_s}, \quad Bi = \frac{\alpha \mathcal{L}}{\mathcal{V}}, \quad k = \frac{\beta C_\infty}{\alpha}. \tag{2.21}$$

Similarly, bulk surfactant equation becomes

$$\frac{\partial C^*}{\partial t^*} + \nabla^* \cdot (C^* \mathbf{U}^*) = \frac{1}{Pe_c} \nabla^* \cdot (D_c^* \nabla^* C^*) - DaBi[C_s^*(k - k\Gamma^*) - \Gamma^*], \tag{2.22}$$

where D_c^* is the nondimensional diffusion coefficient for the bulk surfactant defined as $D_c^* = D_{co}/D_c$. Pe_c and Da are the bulk Peclet number and the Damkohler number, respectively, defined as

$$Pe_c = \frac{\mathcal{V} \mathcal{L}}{D_c}, \quad Da = \frac{\Gamma_\infty}{\mathcal{L} C_\infty}. \tag{2.23}$$

Finally, equation of state in the nondimensional form is

$$\sigma^* = \max \left(\sigma_{min}^*, 1 + E[\ln(1 - \Gamma^*)] \right), \tag{2.24}$$

where σ_{min} and E are the nondimensional surface tension and elasticity number, respectively, defined as

$$\sigma_{min}^* = \frac{\sigma_{min}}{\sigma_s}, \quad E = \frac{\mathcal{R} T \Gamma_\infty}{\sigma_s}. \tag{2.25}$$

2.3   Numerical Method

Treatment of the surface tension, unknown distribution of the surfactant at the interface and at the bulk phase and the moving boundary of the drop render the simulation of interfacial flows in a complex way. In order to solve the problem, the finite difference/front tracking technique developed by Unverdi and Tryggvason [34] is used to solve the flow equations coupled with the interface and bulk surfactant concentration evolution equations. The Navier-Stokes equations, i.e., Eqs. (2.1, 2.2 and 2.4) are solved on a fixed, staggered, Eulerian grid. The spatial derivatives are discretized by using a second order central finite-difference scheme and an explicit, second order projection scheme is used for the time integration.

2.3.1   Staggered Grid System

An accurate approximation of the solution of the partial differential equations requires the splitting of the space and time domains into many small discrete intervals. Instead of obtaining a functional solution to the unknowns, the discrete locations at which the variables are to be calculated are defined by the numerical grid and the unknown values of the variables are obtained by using various numerical techniques. Essentially, this numerical grid is a discrete representation of the geometric domain on which the problem is to be solved. The data structures used to store the information about the grid, the shape of the grid cells and the arrangement of the variables in the grid system are the different options for generating grids. In the contex of this thesis, structured, staggered, Eulerian grid system, which is illustrated in Fig. 2.3, is used. The radial (u_r) and axial (u_z) components of the velocity are stored on the boundaries of the grid cells while the pressure (p) and the rest of the field variables such as denstiy (ρ), viscosity (μ) and bulk surfactant concentration (C) are stored at the cell centroids. Although staggered grid systems developed by Harlow and Welch [37] lead to more complex coding because of the seperate locations of variables, it has an important advantage to couple the pressure to the velocity field, which avoids pressure oscillations and lack of convergence.

●   p, ρ, μ, C

✗ u_r – radial velocity

▲ u_z – axial velocity
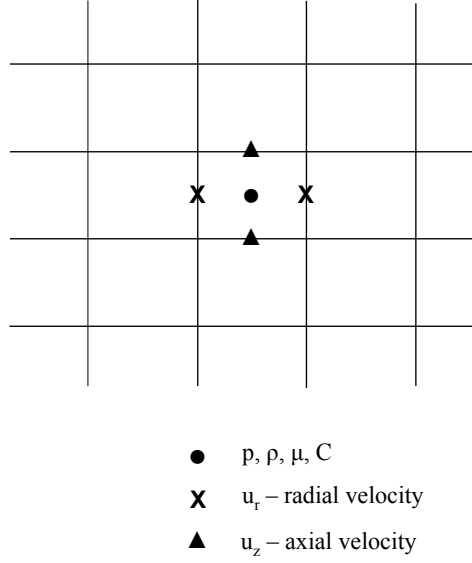
Figure 2.3: Schematic representation of staggered grid system.

2.3.2 Integration of the Flow Equations

Equations (2.1 and 2.2) can be written in a vector form as

$$\frac{\partial}{\partial t}(\rho \mathbf{u}) = \mathbf{A} - \nabla p, \tag{2.26}$$

where $\mathbf{A}$ is

$$\mathbf{A} = -\nabla \cdot (\rho \mathbf{u} \mathbf{u}) + \nabla \cdot \mu (\nabla \mathbf{u} + \nabla \mathbf{u^T}) + \int_A \sigma(\Gamma) \kappa \mathbf{n} \delta(\mathbf{x} - \mathbf{x_f}) \cdot d\mathbf{A}. \tag{2.27}$$

Continuity equation can be written in the form

$$\nabla \cdot \mathbf{u} = 0, \tag{2.28}$$

where $\mathbf{u}$ and ∇ are defined as

$$\mathbf{u} = \{u_r, u_z\}^T, \quad \nabla = \{\frac{\partial}{\partial r}, \frac{\partial}{\partial z}\}^T. \tag{2.29}$$

Then the time discretization of the momentum and continuity equations become

$$\frac{\rho^{n+1} \mathbf{u}^{n+1} - \rho^n \mathbf{u}^n}{\Delta t} = \mathbf{A}_h^n - \nabla_h p, \tag{2.30}$$

$$\nabla_h \cdot \mathbf{u}^{n+1} = 0, \tag{2.31}$$

where n, $n+1$ and h denote the current time level, new time level and the finite-difference approximation to the operator, respectively. As the projection method for the time discretization requires, discretized momentum equation (Eq. (2.30)) is seperated into two parts as follows

$$\frac{\rho^{n+1}\mathbf{u}^* - \rho^n\mathbf{u}^n}{\Delta t} = -\mathbf{A}_h^n, \tag{2.32}$$

$$\frac{\rho^{n+1}\mathbf{u}^{n+1} - \rho^{n+1}\mathbf{u}^*}{\Delta t} = -\nabla_h p. \tag{2.33}$$

Note that $\mathbf{u}^*$ is the unprojected velocity field computed ignoring the effects of pressure field.

In the first step of the projection method, the unprojected velocity field $\mathbf{u}^*$ is seperated from Eq. (2.32), and is computed as

$$\mathbf{u}^* = \frac{1}{\rho^{n+1}}(\rho^n\mathbf{u}^n + \Delta t\mathbf{A}_h^n). \tag{2.34}$$

In the second step, Eq. (2.33) is rearranged as follows

$$\mathbf{u}^{n+1} - \mathbf{u}^* = -\frac{1}{\rho^{n+1}}\Delta t\nabla_h p. \tag{2.35}$$

Then the pressure field is found by taking the divergence of Eq. (2.35) and using the incompressiblity condition given by Eq. (2.31). This leads to

$$\nabla_h \cdot \left(\frac{1}{\rho^{n+1}}\nabla_h p\right) = \frac{1}{\Delta t}\nabla_h \cdot \mathbf{u}^*. \tag{2.36}$$

Equation (2.36) is an elliptic Poisson equation and is solved for the pressure by using a multigrid method described by Tryggvason et al. [38].

In the last step, the velocity field is corrected using the pressure field computed in the second step as

$$\mathbf{u}^{n+1} = \mathbf{u}^* - \frac{1}{\rho^{n+1}}\Delta t\nabla_h p, \tag{2.37}$$

which now satisfies the continuity equation.

2.3.3 Front Tracking Method

Simulation of multiphase flows brings considerable difficulties due to the moving and deforming interface between the two immiscible fluids. The front tracking method used in this

thesis is originally developed by Unverdi and Tryggvason [34]. In this method, the interface between two phases is represented by seperate computational points, i.e., Lagrangian grid, that are moved with the local flow velocity interpolated from the stationary grid. These computational points are called the marker points and a piece of interface between two marker points is called a front element. Figure 2.4 shows a schematic of the computational grids.
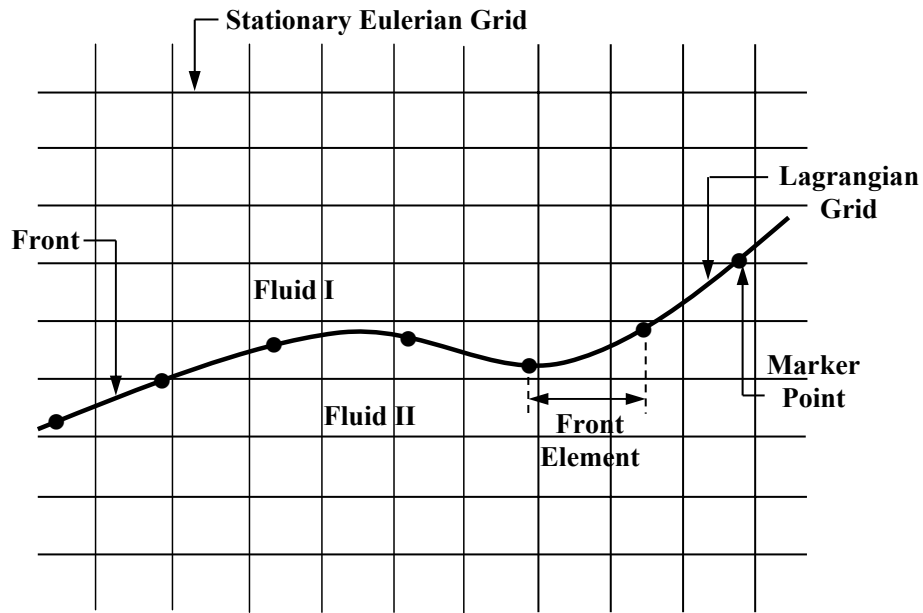
Figure 2.4: Sketch for the computational grids used in the computations of multiphase flows. The governing equations are solved on a stationary Eulerian grid but the interface between the two phases is represented by a Lagrangian grid consisting of connected marker points.

The communication between the marker points and the front elements is provided by linked lists that contain pointers to previous object and the next object in the list. Arbitrary ordering of the data in the list makes the restructuring of the interface easy by allowing the addition and deletion of the elements in some cases.

The restructuring of the front is one of the crucial parts of the front tracking method. Since the drop goes considerable deformation under the effect of the surfactant, there would be a resolution problem for some parts of the front. When the distance between two marker points become too large compared to other points, new elements must be added to maintain

the resolution of the front as sketched in Fig. 2.5. Also, if some parts of the front contains too much front elements, it is possible to delete them by controlling the distance between two neighbouring points or the angle between the two neighbouring front elements. Deletion of these elements reduces the total number of elements used to represent the front as well as prevents the formation of *wiggles* which are much smaller than the grid size. Figure 2.6 illustrates a schematic for a possible element deletion where m, m_p and m_n represent the deleted element, previous element and the next element, respectively.
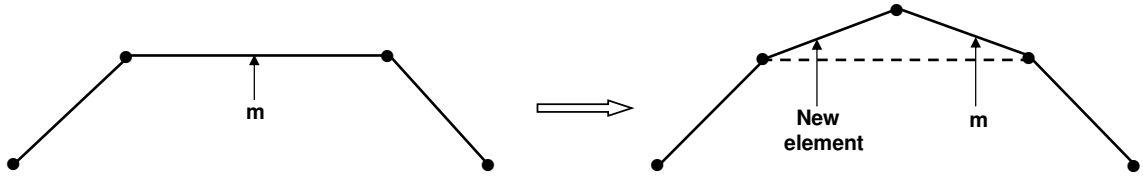
Figure 2.5: Sketch for the element addition while reconstructing the front.
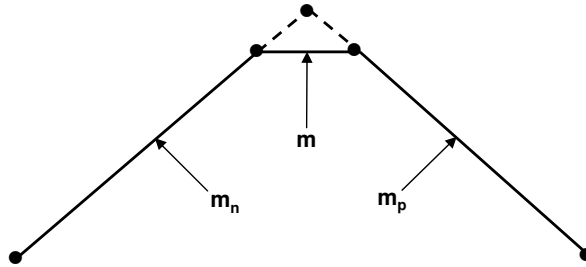
Figure 2.6: Sketch for the element deletion while reconstructing the front.

In addition, in the front tracking method, the density and viscosity fields are not obtained from the direct solution of the equation of state for density and viscosity, i.e., Eq. (2.3). Across the interface, these variables are not continuous and this leads excessive numerical diffusion or some oscillations around the jump. In order to overcome these difficulties, at each time step, position of the interface is used to construct an indicator function defined

as

$$I(r, z, t) = \begin{cases} 1 & \text{in drop fluid} \\ 0 & \text{in bulk fluid.} \end{cases}$$

Since ρ and μ are constant in each phase, proper values of these variables at each grid can be evaluated by using the indicator function such that

$$\rho = \rho_o + (\rho_d - \rho_o)I(r, z, t),$$
$$\mu = \mu_o + (\mu_d - \mu_o)I(r, z, t), \tag{2.38}$$

where the subscripts o and d denotes the bulk and the drop fluids, respectively.

While determining the fluid properties on every grid point, some disturbances may occur due to the length scale equal to the mesh size. In order to avoid this problem around the jump, the interface is given a small thickness of the order of the mesh size, instead of keeping it sharp. The fluid properties change smoothly in this transition zone from the value on one side of the interface to the value on the other side. Since the thickness of the this artificial area is only the function of the mesh size, it stays constant during the calculations and prevents numerical diffusion. Furthermore, by introducing the interface with a finite thickness larger than the mesh size used, it is possible to specify its location exactly. If the indicator function would have taken only the limit values 0 and 1, then it is only possible to state the location of the interface somewhere between the grid points with different values.

The indicator function is computed on the Eulerian grid using the same technique developed by Unverdi and Tryggvason [34]. The method can be outlined briefly in three steps.

In the first step, the discontinuity in the indicator function carried by the interface is distributed onto the grid points adjacent to the interface resulting a gradient field with a finite thickness and is zero except near the interface, i.e.,

$$\mathbf{G}(\mathbf{x}) = \int_A \mathbf{n}\delta(\mathbf{x} - \mathbf{x_f})dA. \tag{2.39}$$

In the second step, divergence of the Eq. (2.39), i.e., $(\nabla_h \cdot \mathbf{G})$, is computed using second order central diferences.

Finally in the third step, the indicator function is evaluated by solving the seperable Poisson equation

$$\nabla^2 I = \nabla_h \cdot \mathbf{G}. \tag{2.40}$$
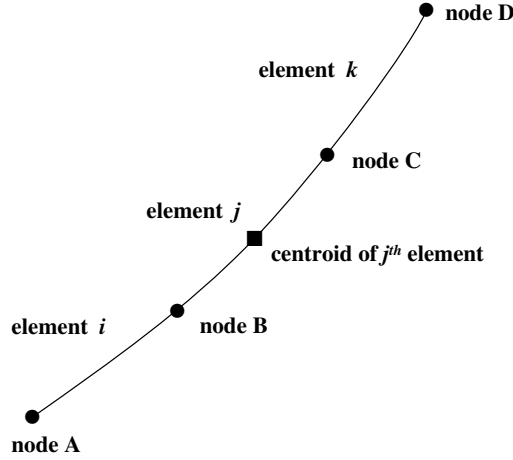
Figure 2.7: Schematic representation of the front elements.

Equation (2.40) is solved efficiently using a fast Poisson solver [39]. The delta function in Eq. (2.39) is approximated by using Peskin's cosine distribution function [36] given by

$$
F(\mathbf{x} - \mathbf{x_f}) = \begin{cases} \frac{1}{(2w)^d} \prod_{i=1}^{d}[1 + cos\frac{\pi}{w}(x_i - (x_f)_i)] & \text{if} & |x_i - (x_f)_i| < w, \quad i = 1, d \\ 0 & \text{otherwise,} \end{cases}
$$

(2.41)

where w is the thickness of the transition zone and d is the dimension, i.e., $d = 2$ for two-dimensional (planar or axisymmetric) problems. The same distribution function is also used to interpolate the velocity field onto the marker points, to distribute the surface tension forces onto the neighbouring grid points and to distribute the surfactant source term computed at the centroids of the front elements. In this thesis, w is taken as $2\Delta x$ for the velocity interpolation and the distribution of surface tension forces onto the neighboring grid points, and as $3\Delta x$ for the distribution of surfactant concentration source term over the adsorption layer.

Surface tension forces at the interface are also computed by using the Lagrangian grid. In order to understand the calculation principle for the surface tension forces, structure of the Lagrangian grid must be understood. Figure 2.7 shows a sketch of the front elements. Connection of the front elements, the node numbers at both ends of an element and the coordinates of all nodes are tracked explicitly in this methodology. For example, element j
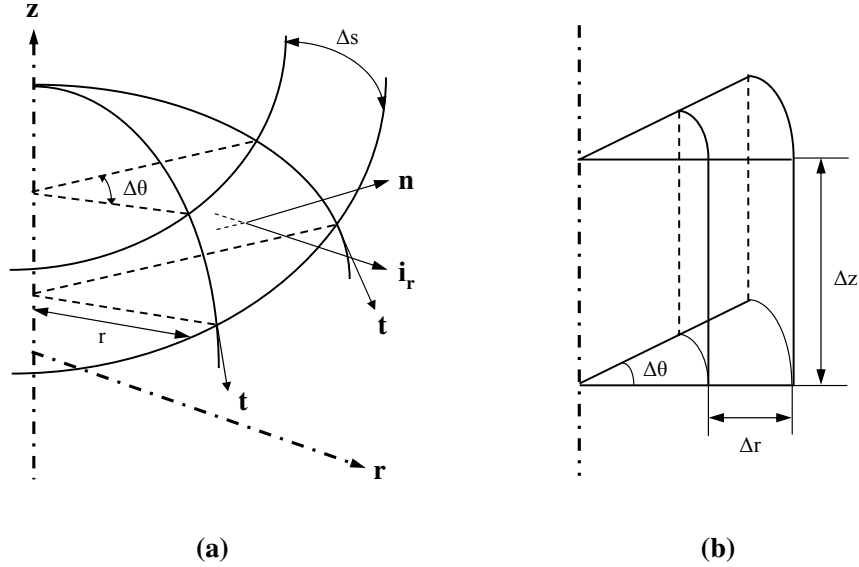
Figure 2.8: (a) A sketch of a boundary element in axisymmetric geometry used for surface tension calculation. (b) Schematic representation of a portion of a surface element.

has two end points, i.e., nodes B and C, along with two neighbouring elements, i.e., elements i and k. The coordinates of all nodes are updated at each time step as the front is advected. The centroid of the element j and the tangent vectors at nodes B and C are computed by fitting a cubic Lagrange polynomial. The force acting on a surface can be written as

$$\Delta F_{ST} = -\int \sigma \kappa \mathbf{n} dS \tag{2.42}$$

where σ is the surface tension that depends on the surfactant concentration, i.e., $\sigma = \sigma(\Gamma)$, κ is the curvature, $\mathbf{n}$ is the normal vector of the surface element, respectively, as shown in Fig. 2.8a. Also, a typical surface element can be seen in Fig. 2.8b. In an axisymmetric geometry, by using above formula, the surface tension force per unit volume can be approximated by

$$\frac{\Delta F_{ST}}{\Delta V} \cong \frac{\Delta(r\sigma\mathbf{t})\Delta\theta\Delta\sigma - \sigma\Delta\theta\Delta s\mathbf{i_r}}{r\Delta r\Delta z\Delta\theta} = \frac{\Delta(r\sigma\mathbf{t}) - \sigma\Delta s\mathbf{i_r}}{r\Delta r\Delta z} \tag{2.43}$$

where r is the radial distance, Δs is the length of the segment ($\Delta s^2 = \Delta r^2 + \Delta z^2$) and $\mathbf{i_r}$ is the radial component of the unit normal vector. Then, as sketched in Fig. 2.9, this force is distributed over the neighbouring Eulerian grid cells as body forces in a conservative
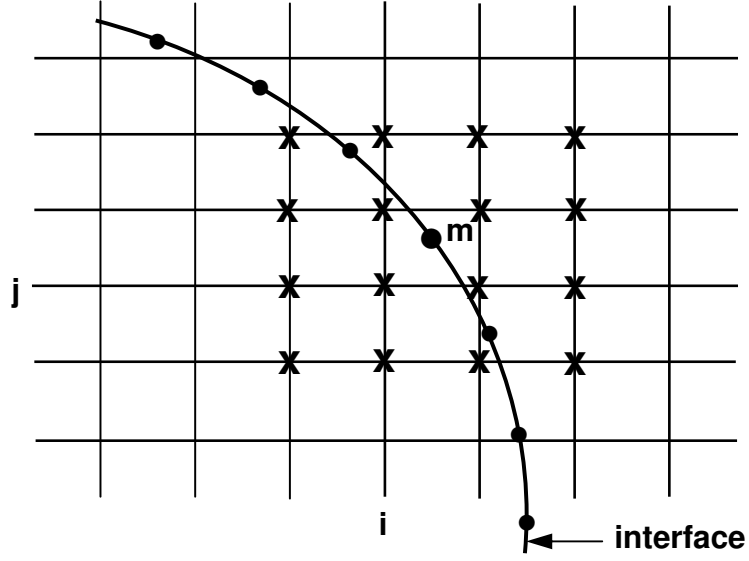
Figure 2.9: Schematic representation of the distribution of surface tension force and velocity interpolation schemes, involving 16 grid points.

manner using Peskin's distribution function. Surface tension force F_{ST} is involved in the computation of velocity field and the velocity is interpolated onto the location of mth marker point from 16 neighbouring Eulerian grid nodes as well as the the surface tension forces computed at front element centroids (not shown on the sketch above) are distributed onto 16 neighbouring Eulerian grid nodes.

2.3.4   Integration of the Surfactant Evolution Equation at the Interface

The convection/diffusion equation for surfactant at the interface is solved in dimensional form on a Lagrangian grid. From Eq. (2.8) and Eq. (2.9), we obtain

$$\frac{\partial \Gamma}{\partial t} + \nabla \cdot (\Gamma \mathbf{U_s}) - \Gamma \mathbf{n} \cdot \nabla \mathbf{U_s} \cdot \mathbf{n} = D_s \nabla_s^2 \Gamma + \dot{S_\Gamma}. \tag{2.44}$$

On the other hand, an area element of the interface evolves by [32]

$$\frac{DA}{Dt} = \frac{\partial A}{\partial t} + \mathbf{U_s} \cdot \nabla A = -A(\mathbf{n} \cdot \nabla U_s \cdot \mathbf{n}). \tag{2.45}$$

Combining Eq. (2.44) and Eq. (2.45), we get

$$\frac{d\Gamma A}{dt} = AD_s \nabla_s^2 \Gamma + A\dot{S_\Gamma}. \tag{2.46}$$

In an axisymmetric problem, Eq. (2.46) becomes

$$\frac{d\Gamma A}{dt} = A[D_s \frac{1}{r} \frac{\partial}{\partial s}(r \frac{\partial \Gamma}{\partial s}) + \dot{S}_\Gamma]. \tag{2.47}$$

Equation (2.47) can be expressed as

$$\frac{d\Gamma A}{dt} = Af(\Gamma, t), \tag{2.48}$$

where function f is defined as

$$f(\Gamma, t) = A[D_s \frac{1}{r} \frac{\partial}{\partial s}(r \frac{\partial \Gamma}{\partial s}) + \dot{S}_\Gamma]. \tag{2.49}$$

A central difference scheme is used to approximate Eq. (2.49) as

$$[Af]_k \cong \frac{A_k}{r_k} D_s [\frac{r_{k+\frac{1}{2}} \frac{\Gamma_{k+1}-\Gamma_k}{s_{k+1}-s_k} - r_{k-\frac{1}{2}} \frac{\Gamma_k-\Gamma_{k-1}}{s_k-s_{k-1}}}{s_{k+\frac{1}{2}} - s_{k-\frac{1}{2}}}] + A_k \dot{S}_{\Gamma_k}, \tag{2.50}$$

where k denotes the kth front element. Figure 2.10 shows the details of the elements used in the spatial discretization of the surfactant concentration evolution equation. Surface area of an element can be approximated as

$$A_k \cong \frac{1}{2}(r_{k+\frac{1}{2}} + r_{k-\frac{1}{2}})\Delta s_k \cong r_k \Delta s_k, \tag{2.51}$$

where $\Delta s_k = s_{k+\frac{1}{2}} - s_{k-\frac{1}{2}}$. Then Eq. (2.50) becomes

$$[Af]_k \cong D_s [\frac{r_{k+\frac{1}{2}} \frac{\Gamma_{k+1}-\Gamma_k}{\Delta s_{k+\frac{1}{2}}} - r_{k-\frac{1}{2}} \frac{\Gamma_k-\Gamma_{k-1}}{\Delta s_{k-\frac{1}{2}}}}{2r_k}](r_{k+\frac{1}{2}} + r_{k-\frac{1}{2}}) + A_k \dot{S}_{\Gamma_k}. \tag{2.52}$$

Time integration is performed using an explicit Euler scheme as

$$\Gamma^{n+1} = \frac{1}{A^{n+1}}[\Gamma^n A^n + \Delta t A^n f(\Gamma^n, t^n)]. \tag{2.53}$$

The second order time accuracy is recovered using the methodology as explained in Section 2.3.6, which corresponds to a trepozoidal rule.

2.3.5 Integration of the Bulk Surfactant Concentration Evolution Equation

The bulk surfactant concentration equation, i.e., Eq. (2.11), is solved on the staggered Eulerian grid where the bulk surfactant concentration is stored at the cell centroids. The spatial derivative for the diffusive flux is approximated by using second order central differences. An ENO (essentially nonoscillatory) algorithm [40, 41] is used for the convective
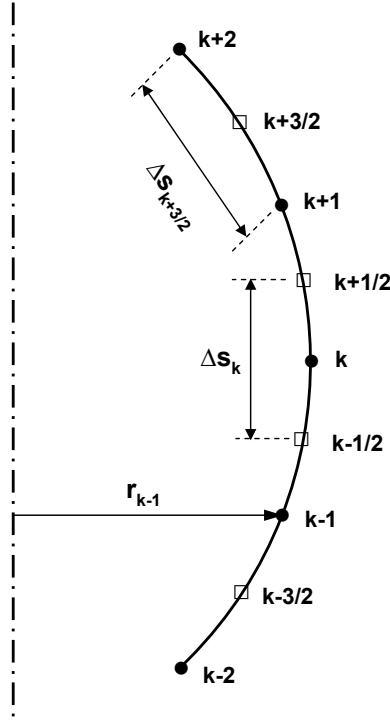
Figure 2.10: Sketch for the spatial discretization of the surfactant evolution equation. The circles corresponds to the Lagrangian marker points while the squares represents the front element centroids.

terms in order to avoid oscillations near the interface due to large gradients. Let $C_{i,j}$ and $\mathbf{u}_{i,j}$ be the discrete values of bulk concentration and the velocity at $r = r_i$ and $z = z_j$, then, Eq. (2.11) is rewritten in axisymmetric geometry to yield

$$\frac{\partial C}{\partial t} + u_r \frac{\partial C}{\partial r} + u_z \frac{\partial C}{\partial z} = \frac{1}{r} \frac{\partial}{\partial r}(r D_{co} \frac{\partial C}{\partial r}) + \frac{\partial}{\partial z}(D_{co} \frac{\partial C}{\partial z}) + \dot{S_C}. \tag{2.54}$$

The semi-discrete version of Eq. (2.54) is

$$\left(\frac{dC}{dt}\right)_{ij} = R_{C_{i,j}} + R_{D_{i,j}} + R_{S_{i,j}} = \text{Res}_{i,j}, \tag{2.55}$$

where R_C, R_D, R_S denote the convective, diffusive and source terms, respectively, and are given by

$$R_{C_{i,j}} = -\left(u_r\frac{\partial C}{\partial r} + u_z\frac{\partial C}{\partial z}\right)_{i,j},$$

$$R_{D_{i,j}} = \left(\frac{1}{r}\frac{\partial}{\partial r}(rD_{co}\frac{\partial C}{\partial r}) + \frac{\partial}{\partial z}(D_{co}\frac{\partial C}{\partial z})\right)_{i,j},$$

$$R_{S_{i,j}} = \left(\dot{S}_C\right)_{i,j}. \tag{2.56}$$

Discretization of the Convective Terms

The convective terms are discretized using an essentially nonoscillatory (ENO) scheme [40, 41] as follows

$$R_{C_{i,j}} = -(u_{r_{i,j}} + u_{r_{i-1,j}})\frac{C_{i+1/2,j} - C_{i-1/2,j}}{\Delta r} - (u_{z_{i,j}} + u_{z_{i,j-1}})\frac{C_{i,j+1/2} - C_{i,j-1/2}}{\Delta z}. \tag{2.57}$$

The values of C at the cell boundaries are computed as

$$C_{i+1/2,j} = \begin{cases} C_{i,j} + \frac{1}{2}F(D_x^+C_{i,j}, D_x^-C_{i,j}) & \text{if } \mathbf{u}_{i,j} > 0 \\ C_{i+1,j} - \frac{1}{2}F(D_x^+C_{i+1,j}, D_x^-C_{i+1,j}) & \text{if } \mathbf{u}_{i,j} < 0 \end{cases}, \tag{2.58}$$

where the differences are found by $D_x^+C_{i,j} = C_{i+1,j} - C_{i,j}$ and $D_x^-C_{i,j} = C_{i,j} - C_{i-1,j}$. Also, F is a function defined by

$$F(a,b) = \begin{cases} a, & |a| < |b| \\ b, & |b| \leqslant |a| \end{cases} \tag{2.59}$$

Discretization of the Diffusive Terms

Diffusive terms are approximated using central differences as

$$\begin{aligned} \left(\frac{1}{r}\frac{\partial}{\partial r}(rD_{co}\frac{\partial C}{\partial r})\right)_{i,j} &= \frac{(rD_{co})_{i+1/2,j}(\frac{\partial C}{\partial r})_{i+1/2,j} - (rD_{co})_{i-1/2,j}(\frac{\partial C}{\partial r})_{i-1/2,j}}{r_{i,j}\Delta r} \\ &= \frac{(rD_{co})_{i+1/2,j}\frac{C_{i+1,j}-C_{i,j}}{\Delta r} - (rD_{co})_{i-1/2,j}\frac{C_{i,j}-C_{i-1,j}}{\Delta r}}{r_{i,j}\Delta r} \\ &= [\frac{(rD_{co})_{i+1,j} + (rD_{co})_{i,j}}{2r_{i,j}}](\frac{C_{i+1,j} - C_{i,j}}{\Delta r^2}) \\ &\quad -[\frac{(rD_{co})_{i,j} + (rD_{co})_{i-1,j}}{2r_{i,j}}](\frac{C_{i,j} - C_{i-1,j}}{\Delta r^2}). \end{aligned} \tag{2.60}$$

$$
\begin{aligned}
\left(\frac{\partial}{\partial z}(D_{co}\frac{\partial C}{\partial z})\right)_{i,j} &= \frac{D_{co_{i,j+1/2}}(\frac{\partial C}{\partial z})_{i,j+1/2} - D_{co_{i,j-1/2}}(\frac{\partial C}{\partial z})_{i,j-1/2}}{\Delta z} \\
&= \frac{D_{co_{i,j+1/2}}\frac{C_{i,j+1}-C_{i,j}}{\Delta z} - D_{co_{i,j-1/2}}\frac{C_{i,j}-C_{i,j-1}}{\Delta z}}{\Delta z} \\
&= [\frac{D_{co_{i,j+1}} + D_{co_{i,j}}}{2}](\frac{C_{i,j+1} - C_{i,j}}{\Delta z^2}) \\
&\quad -[\frac{D_{co_{i,j}} + D_{co_{i,j-1}}}{2}](\frac{C_{i,j} - C_{i,j-1}}{\Delta z^2}).
\end{aligned}
\tag{2.61}
$$

Treatment of the Source Term

The source term is first computed at the centroids of front elements and then distributed over the adsorption layer using a modified version of Peskin's distribution function given by

$$
F_c(\mathbf{x}-\mathbf{x_f}) = \begin{cases} \prod_{i=1}^{d}[1 + \cos\frac{\pi}{w}(x_i - (x_f)_i)] & \text{if} \quad |x_i - (x_f)_i| < w, I \leqslant 0.5, \quad i = 1, d \\ 0 & \text{otherwise,} \end{cases}
\tag{2.62}
$$

Figure 2.11 shows the schematic illustration of the interpolation scheme for the bulk surfactant concentration. The bulk surfactant concentration is interpolated onto the kth front element from the Eulerian grid nodes outside the drop, i.e., the nodes circled in the sketch. Furthermore, the source term computed on the front element is distributed onto the same Eulerian grid nodes.

The time integration is performed using either a first order or second order explicit schemes. First order scheme is the explicit Euler method given by

$$
C_{i,j}^{n+1} = C_{i,j}^n + \Delta t \text{Res}_{i,j}^n.
\tag{2.63}
$$

The second order time integration is explained in the following section.

2.3.6   Overall Solution Procedure

A two-stage algorithm is used to combine the finite difference and front tracking methods. The first stage yields first order accurate integration in time and the combination of first and second stages yields a second order accuracy in time in advancing solutions from physical time level n ($t_n = \sum_{i=1}^{n} \Delta t_i$) to level $n + 1$. The overall solution procedure can be summarized as follows:
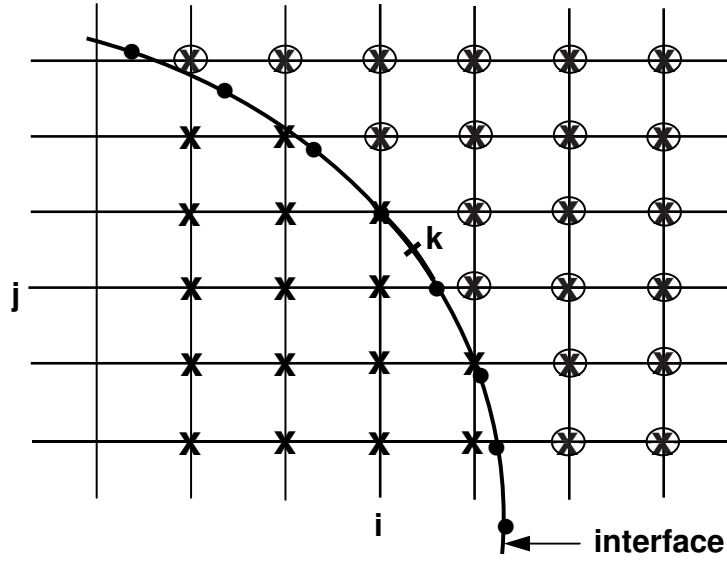
Figure 2.11: Sketch for the interpolation scheme for the bulk surfactant concentration.

- The positions of the marker points are advanced using first order Euler method, i.e.,

$$\mathbf{X}_p^{n+1} = \mathbf{X}_p^n + \Delta t \mathbf{V}_p^n, \tag{2.64}$$

where $\mathbf{V}_p^n$ is the velocity vector interpolated on the marker point p.

- The bulk and interface surfactant concentrations are advanced for a single time step as explained in previous sections.

- The material properties and surface tension are computed based on the new front locations as

$$\rho^{n+1} = \rho(\mathbf{X}_p^{n+1}), \quad \mu^{n+1} = \mu(\mathbf{X}_p^{n+1}), \quad \sigma^{n+1} = \sigma(\Gamma^{n+1}). \tag{2.65}$$

- The pressure field and the velocity field are computed from Eq. (2.36 and 2.37), respectively.

- In order to obtain second order accuracy in time, the procedure above is repeated once again and the solutions are computed at time level $n + 2$. Then the quantities

are updated using simple avarages as follows:

$$
\begin{aligned}
\mathbf{X_p}^{n+1} &= \frac{1}{2}\left(\mathbf{X_p}^{n} + \mathbf{X_p}^{n+2}\right), \\
\mathbf{V}^{n+1} &= \frac{1}{2}\left(\mathbf{V}^{n} + \mathbf{V}^{n+2}\right), \\
\Gamma^{n+1} &= \frac{1}{2}\left(\Gamma^{n} + \Gamma^{n+2}\right), \\
C^{n+1} &= \frac{1}{2}\left(C^{n} + C^{n+2}\right), \\
\rho^{n+1} &= \frac{1}{2}\left(\rho^{n} + \rho^{n+2}\right), \\
\mu^{n+1} &= \frac{1}{2}\left(\mu^{n} + \mu^{n+2}\right), \\
\sigma^{n+1} &= \frac{1}{2}\left(\sigma^{n} + \sigma^{n+2}\right).
\end{aligned}
\tag{2.66}
$$

2.4   Drop Breakup Mechanism

A liquid droplet can cleave with the help of the surface tension forces. In order to simulate the behaviour of the viscous droplets under the influence of the soluble surfactants, a drop breakup mechanism developed by Olgac et al. [2] is used. In this methodology, during the evolution of the drop necking process, the radius of the neck is monitored and when it becomes smaller than a threshold value R_{break}, the neighbouring marker points of the front element that is closest to the centerline are projected onto the centerline as shown in Fig. 2.12. As can be seen in this figure, these newly found marker points are the new boundary points for the daughter droplets. After that, the front element is deleted and the volume of the droplets are updated. The threshold value for the critical neck radius is taken to be $0.75\Delta y$ where Δy is the grid size in z- direction in cylindirical coordinates.
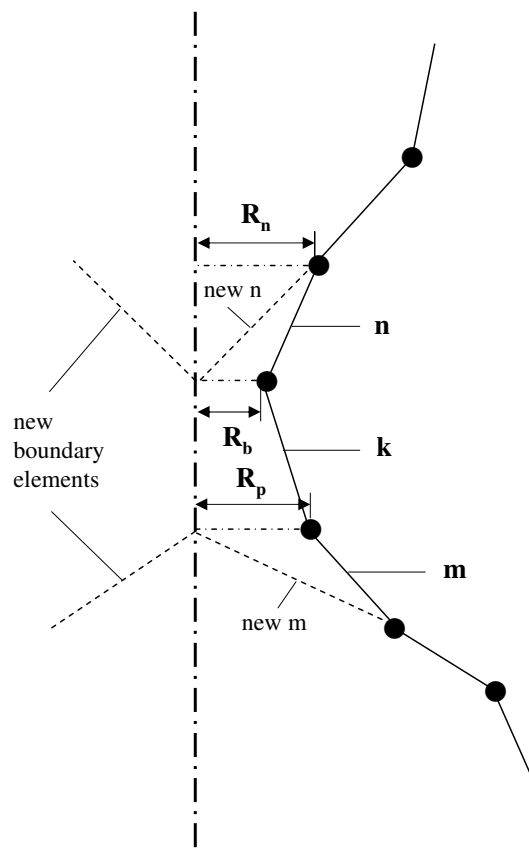
Figure 2.12: Sketch for the drop breakup mechanism. The marker points at both ends of the kth element are projected onto the centerline when R_b is smaller than the critical neck radius R_{break}, front element k is deleted and new boundary elements are created [2].

Chapter 3

VALIDATION OF THE NUMERICAL ALGORITHM

A number of test cases are performed to validate the numerical solution algorithm. The flow solver and the FD/FT method have been validated many times before for surfactant-free cases [38], so tests are performed here only for the cases with surfactant. For this purpose, each term in Eq. (2.11) and Eq. (2.46) is tested individually and results are compared with the analytical solutions for the simple test cases.

3.1 Surfactant Convection Test

First a simple test case is considered to validate the numerical approximation to the convective terms in Eq. (2.46). As sketched in Fig. 3.1, the interface is initialized as a sphere and located at the center of the computational domain on the axis of symmetry with a uniform initial surfactant distribution. The spherical interface continuously expands in the normal direction with a constant radial velocity. Both the diffusion and the source terms are neglected so the surfactant concentration evolution only depends on the change in the surface area of the drop. Thus Eq. (2.46) reduces to

$$\frac{d\Gamma A}{dt} = 0, \tag{3.1}$$

which can be integrated in time to yield

$$\Gamma^*(t) = \frac{A_o}{A(t)}\Gamma_o^*, \tag{3.2}$$

where Γ^* is the dimensionless time dependent surfactant concentration given by $\Gamma^* = \Gamma/\Gamma_\infty$. A_o, $A(t)$ and Γ_o^* are the initial surface area of the drop, the surface area of the drop at time t and the dimensionless initial surfactant concentration, respectively. The numerical and analytical solutions for the evolution of the surfactant concentration at the drop interface is plotted in Fig. 3.2. As it is seen in this figure, the numerical results are in excellent agreement with the analytical solution indicating the accurate discretization of the convective terms in surfactant evolution equation.
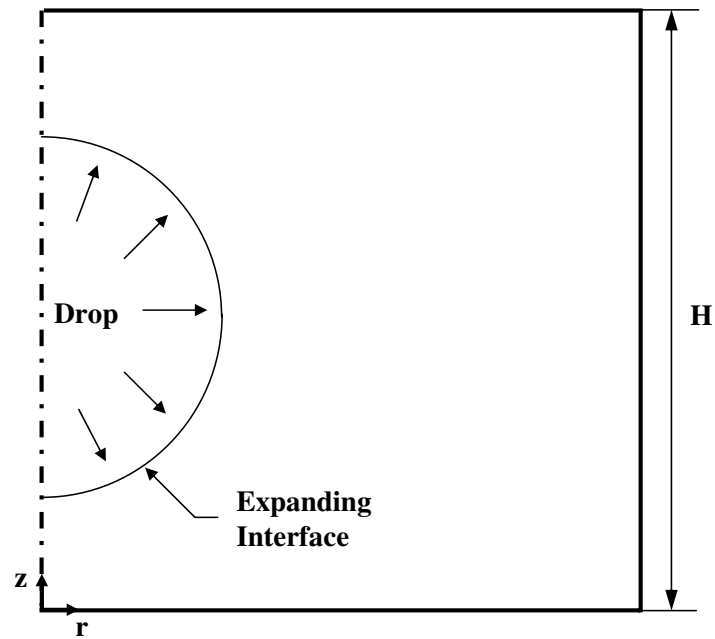
Figure 3.1: Schematic representation of the computational domain used to test the convective terms in surfactant evolution equation.
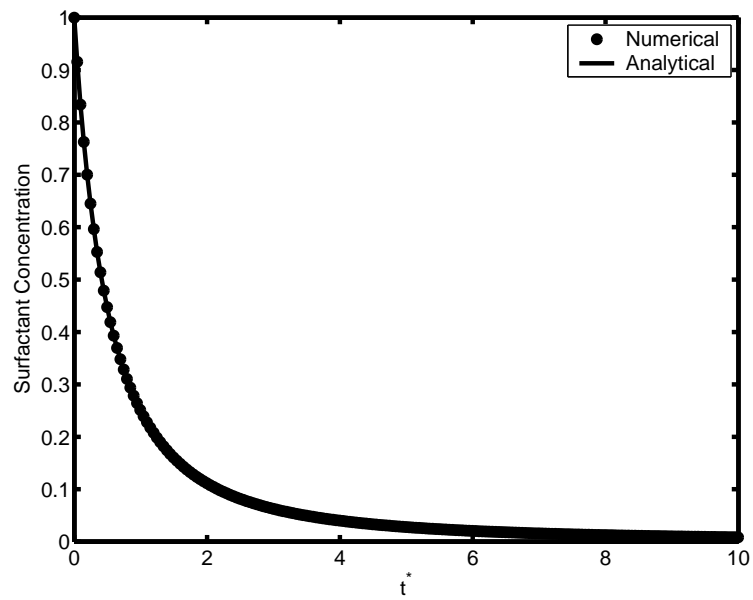
Figure 3.2: Evolution of the surfactant concentration for a continuously expanding spherical interface when the diffusion and the source terms are neglected.

3.2 Surfactant Diffusion Test at the Interface

In this test case, a spherical interface of radius a is kept stationary, velocity is fixed zero and the source term $\dot{S}_\Gamma$ is switched off. The nonuniform initial surfactant concentration is specified as

$$\Gamma = \frac{1}{2}(1 - cos\theta), \tag{3.3}$$

where θ is the angle measured in clockwise direction. Figure 3.3 shows the initial surfactant distribution over the interface. In this figure, the solid line shows the drop interface while the dotted line is the initial surfactant concentration. As can be seen in the figure, the drop is placed at the center of the axis of symmetry represented by the dashed dot line. In this case, Eq. (2.46) reduces to

$$\frac{\partial \Gamma}{\partial t} = \frac{D_s}{r}\frac{\partial}{\partial s}(r\frac{\partial \Gamma}{\partial r}). \tag{3.4}$$

Figure 3.3: Initial surfactant distribution on the drop interface for diffusion test. The solid line denotes the interface while the dotted line denotes the initial surfactamt distribution.

Since the drop is stationary, i.e., $r = $ constant, Eq. (3.4) simplifies to be

$$\frac{\partial \Gamma}{\partial t} = D_s \frac{\partial^2 \Gamma}{\partial \theta^2}, \tag{3.5}$$

which can be solved analytically to yield
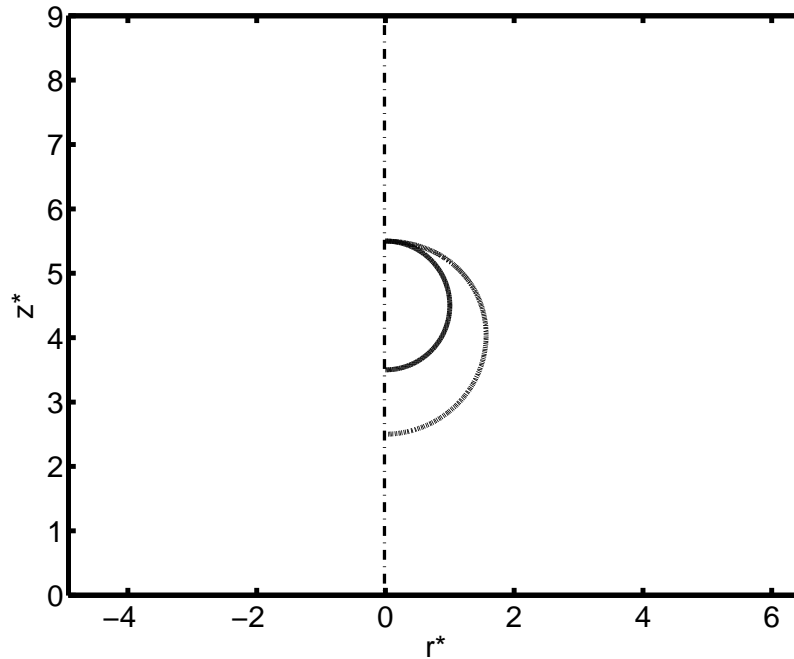
$$\Gamma(\theta, t) = \frac{1}{2}\left(1 - e^{-\frac{2t^*}{Pe_s}} \cos\theta\right). \tag{3.6}$$

In Eq. (3.5), Pe_s is the surface Peclet number defined as $Pe_s = \mathcal{V}a/D_s$, t^* is the dimensionless time defined as $t^* = t\mathcal{V}/a$ and $\mathcal{V}$ is a velocity scale. The numerical results are compared with the analytical solutions for two cases. First Pe_s is kept constant and the evolution of the surfactant concentration at various nondimensional time frames is taken into account. As can be seen in Fig. 3.4, surface diffusion process acts to distribute the surfactant uniformly onto the surface and the numerical results are in good agreement with the analytical solutions in all time frames. Second surfactant concentration profiles for various Pe_s are examined at a constant time. As Pe_s reduces, surface diffusion becomes dominant and the surfactant concentration tends to distribute uniformly. As shown in Fig. 3.5, the numerical results also match very well with the analytical solution for this case indicating the accurate discretization of the diffusive terms.

Grid convergence analysis is also performed for the interface diffusion scheme for surfactant. The surfactant concentration at the interface at a constant time is plotted in Fig. 3.6 and compared with the analytical solution. The computations are performed for various grid resolutions ranging between 16×48 and 256×768. As can be seen in this figure, the computational results converge to the analytical solution as the computational grid is refined. Moreover surfactant concentrations of two locations corresponding to $s = 0.35$ and $s = 0.65$ are plotted against the square of the grid size, i.e., Δx^2, in order to determine the degree of accuracy. As it is clearly seen in Fig. 3.7, the diffusion scheme is second order accurate in space. In this figure, symbols represents the computational results for various grids and the solid lines are the least square fits to the computational data.

3.3 Surface Adsorption/Desorption Test

In order to test the adsorption-desorption scheme for the source term, interface is kept stationary by setting the velocity field to zero and diffusion term is switched off. In addition,
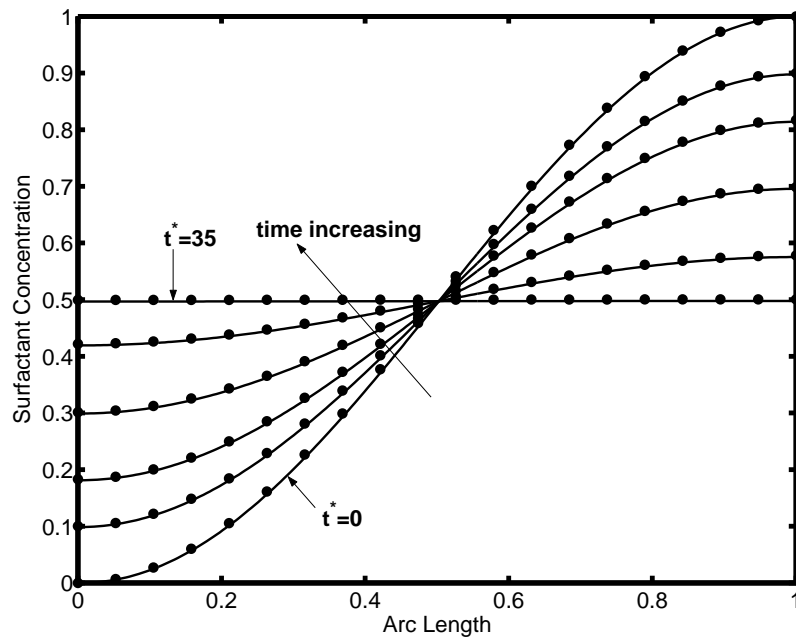
Figure 3.4: Surfactant concentration Γ evolution on the drop surface for Pe_s=10. Solid lines are the numerical solutions and the filled circles denotes the analytical solutions.
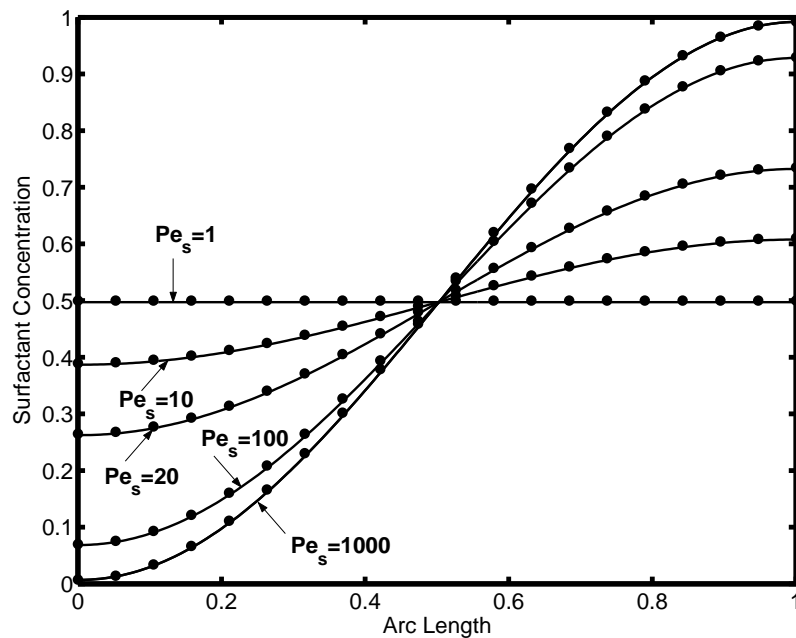
Figure 3.5: Surfactant concentration Γ as a function of normalized arc length s for various Pe_s numbers at $t^* = 8$. Solid lines are the numerical solutions and the filled circles denotes the analytical solutions.
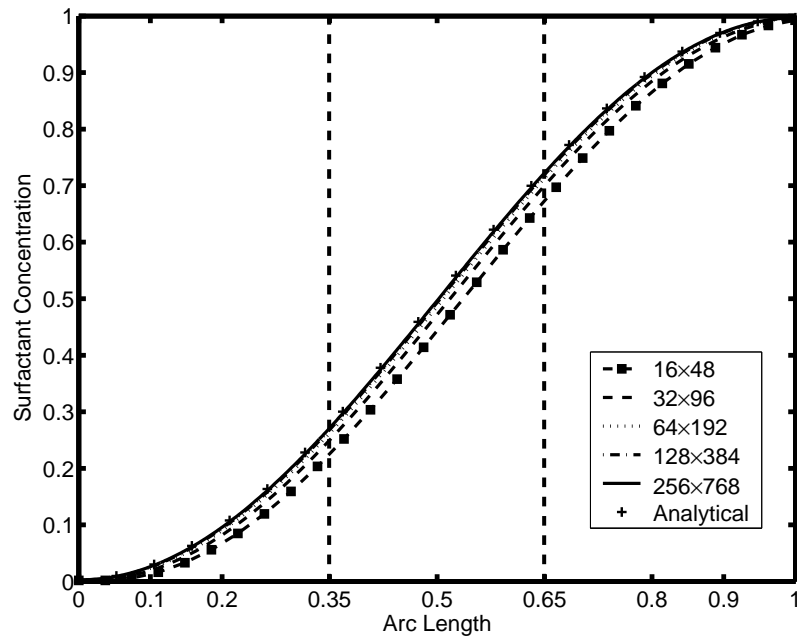
Figure 3.6: Surfactant concentration Γ as a function of normalized arc length s for various grid resolutions at $t^* = 2.90$ at $Pe_s = 1000$.

Figure 3.7: Surfactant concentration versus Δx^2 at the front locations corresponding to $s = 0.35$ and $s = 0.65$.

the bulk surfactant concentration C is kept constant at unity. In this case, Eq. (2.46) reduces to

$$\frac{d\Gamma}{dt} = \beta(\Gamma_\infty - \Gamma) - \alpha\Gamma, \qquad (3.7)$$

which can be integrated in time to obtain the analytical solution given by

$$\Gamma^* = \frac{\beta/\alpha}{1 + \beta/\alpha}[1 - e^{-(1+\beta/\alpha)\text{Bi}t^*}]. \qquad (3.8)$$

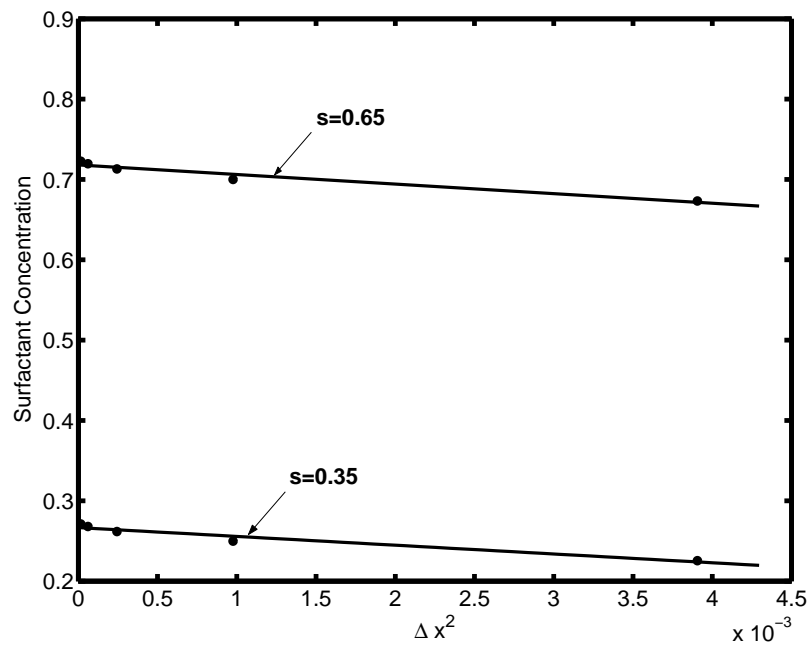Initially, there is no surfactant at the drop interface and since the diffusive and convective terms are neglected, the interface surfactant concentration Γ only depends on the source term. As it can be seen in Fig. 3.8, numerical and analytical solutions for different Biot numbers are considered. At high Biot numbers, mass transfer rate is higher and surfactant is deposited onto the surface faster. As the Biot number increases, numerical and analytical solutions start to differ due to the large time-stepping error. However, when the Biot number decreases, numerical results match much better with the analytical solution as can be seen in Fig. 3.8. Also, for high Biot numbers, when the time step is reduced, numerical results approaches to the analytical solution as shown in Fig. 3.9. The ratio of adsorption and desorption coefficients, i.e., β/α, is taken 4.0 in both cases.
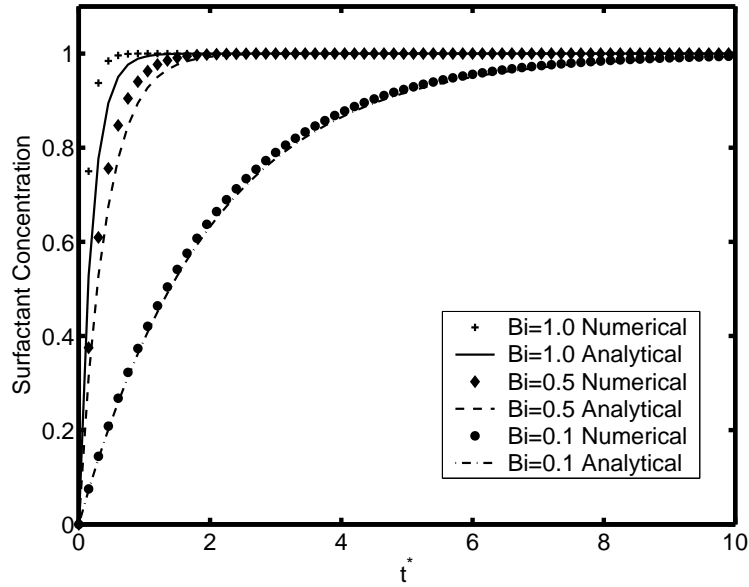

Figure 3.8: Evolution of the surfactant concentration at the interface when the diffusive and convective terms are neglected. ($\Delta t^* = 0.15$, $\beta/\alpha = 4.0$)
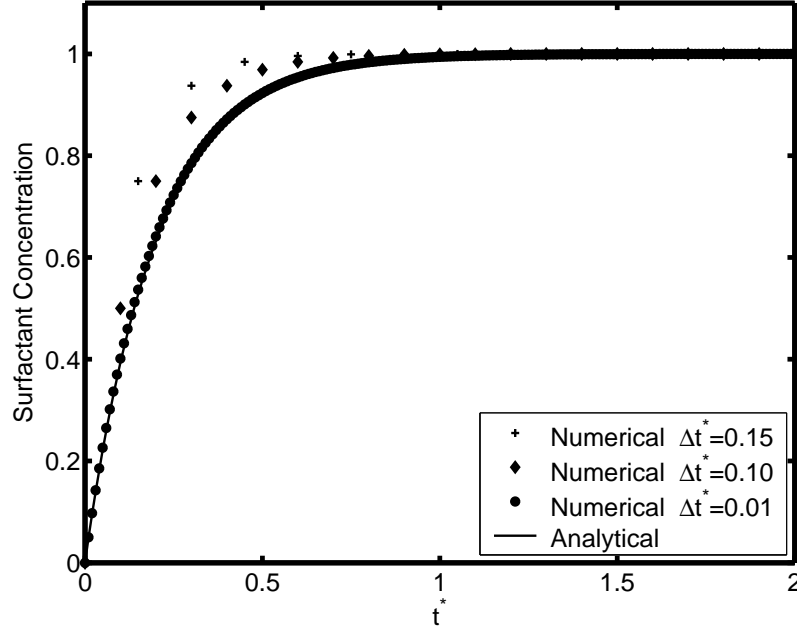
Figure 3.9: Evolution of the surfactant concentration at the interface for different time steps when the diffusive and convective terms are neglected. ($Bi = 1.0$, $\beta/\alpha = 4.0$)

3.4 Bulk Surfactant Diffusion and Mass Transfer Test

In this section, bulk surfactant diffusion and the mass transfer between the bulk and the drop interface is tested. A stationary spherical droplet with radius a is placed at the center of a cylindirical tube on the axis of symmetry as sketched in Fig. 3.10. Initially, there is no surfactant at the drop interface, i.e., $\Gamma_o = 0$, and the initial bulk surfactant concentration is uniform, i.e., $C = C_\infty$. Mass transfer is only due to the moleculer diffusion. In addition, desorption coefficient is taken zero, i.e., $\alpha = 0$, so mass transfer is always from the bulk fluid to the drop interface. Under these conditions, the source term is simply given by

$$\dot{S}_\Gamma = \beta C_s. \tag{3.9}$$

And the bulk surfactant evolution equation becomes

$$\frac{\partial C}{\partial t} = \frac{D_c}{r^2}\frac{\partial}{\partial}(r^2\frac{\partial C}{\partial r}), \tag{3.10}$$

which can be solved analytically for short times or in infinite domain to yield

$$C = C_\infty[1 - \frac{\beta\sqrt{\pi D_c t}/D_c}{1 + \frac{\sqrt{\pi D_c t}}{a}(1 + \frac{\beta a}{D_s})}\frac{r}{a}\text{erfc}\left(\frac{r - a}{2\sqrt{D_c t}}\right)], \tag{3.11}$$

where erfc(x) is the complementary error function. The surfactant concentration equation at the interface becomes

$$\frac{d\Gamma}{dt} = \beta C_s|_{r=a}. \tag{3.12}$$

Using Eq. (3.11), Eq. (3.12) can be solved for the surfactant concentration at the interface and it is given by

$$\Gamma = \Gamma_o + \beta C_\infty [t - \frac{wh}{\eta^3}(\eta^2 t - 2\eta\sqrt{t} + 2\ln(1 + \eta\sqrt{t}))], \tag{3.13}$$

where Γ_o is the initial surfactant concentration at the interface, $w = \frac{\beta}{D_c}$, $h = \sqrt{\pi D_c}$ and $\eta = \frac{h}{a}(1 + wa)$. In this test case, computational domain is resolved by a uniform Cartesian grid
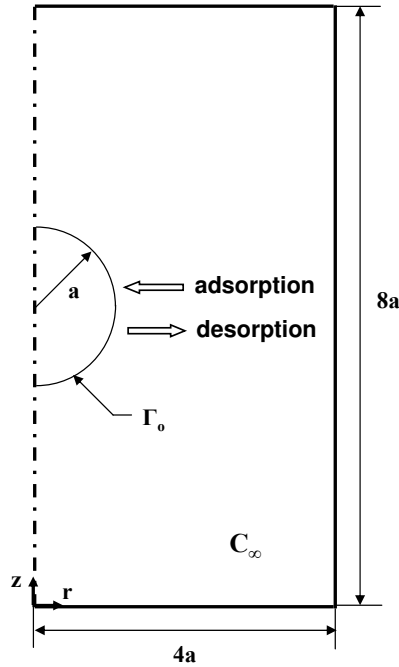
Figure 3.10: Schematic representation of the computational domain used in testing the bulk surfactant diffusion and mass transfer rate.

containing 128×256 grid cells. Bulk surfactant Peclet number is taken as $Pe_c = 1000$ and the diffusion of the surfactant at the interface is neglected. So the accumulation of the surfactant is only due to the adsorption-desorption process. All variables are nondimensionalized by using the length scale $\mathcal{L} = a$ and the time scale $\mathcal{T} = a^2/D_c$.

Time evolution of the bulk surfactant concentration is shown in Fig. 3.11. In these figures, the contour plots of the bulk surfactant concentration are plotted at various time

frames. As can be seen in these figures, the spherical symmetry of the bulk surfactant concentration contours are almost perfect and they continue until the propogation of the diffusive effect of the bulk surfactant arrives at the solid boundary of the cylindirical tube. This spherical symmetry indicates the accuracy of the computational results.

Bulk surfactant concentration profiles along the horizontal plane passing through the center of the computational domain are plotted in Fig. 3.12 and compared with the analytical solution. As can be seen in this figure, computational results match very well with the analytical solution except for the regions very close to the drop tip and the east boundary of the domain. In the region near the drop interface, bulk surfactant concentration gradient variations are very severe leading to large numerical errors, and in the regions very close to the east solid boundary of the domain, analytical solution is not valid so that it differs from the numerical solution at this region.

Furthermore surfactant concentration profiles on the drop interface at various time frames are compared with the analytical solution in Fig. 3.13. Although some oscillations are observed as the time increases at the computationally found interface surfactant concentrations, numerical solutions are very close to the analytical solutions.

Finally a grid convergence test is carried out for the surface concentration with adsorption. As shown in Fig. 3.14, as the grid is refined from 16×32 to 128×256, the solution for the surfactant concentration at the interface Γ is seen to converge to the analytical solution given by Eq. (3.13).

Figure 3.11: Diffusion test for the bulk surfactant concentration. Bulk surfactant concentration contours at $t^* = 0.0037$, $t^* = 0.4875$, $t^* = 1.3312$ and $t^* = 3.1125$. Time progress from left to right and top to bottom.
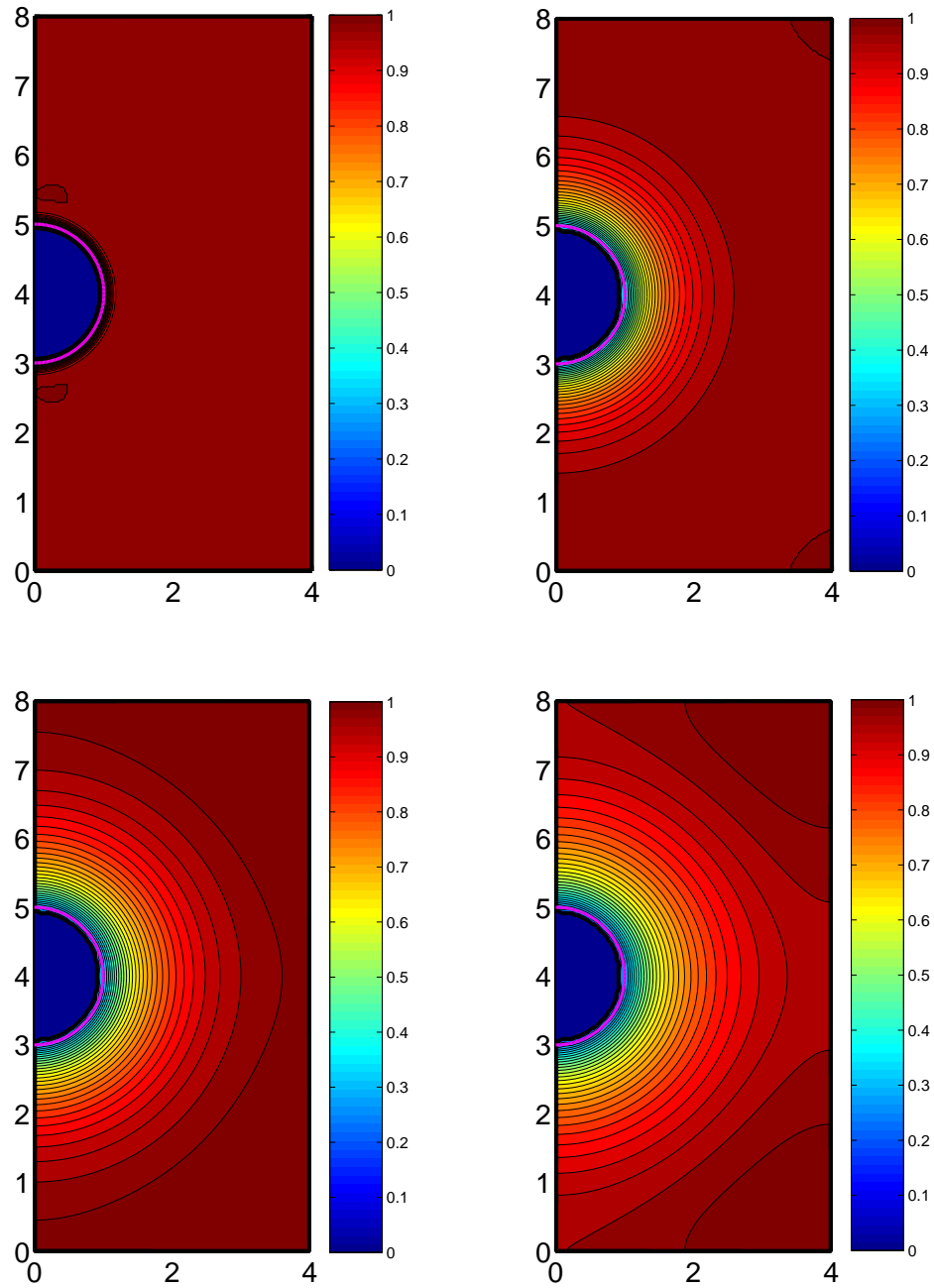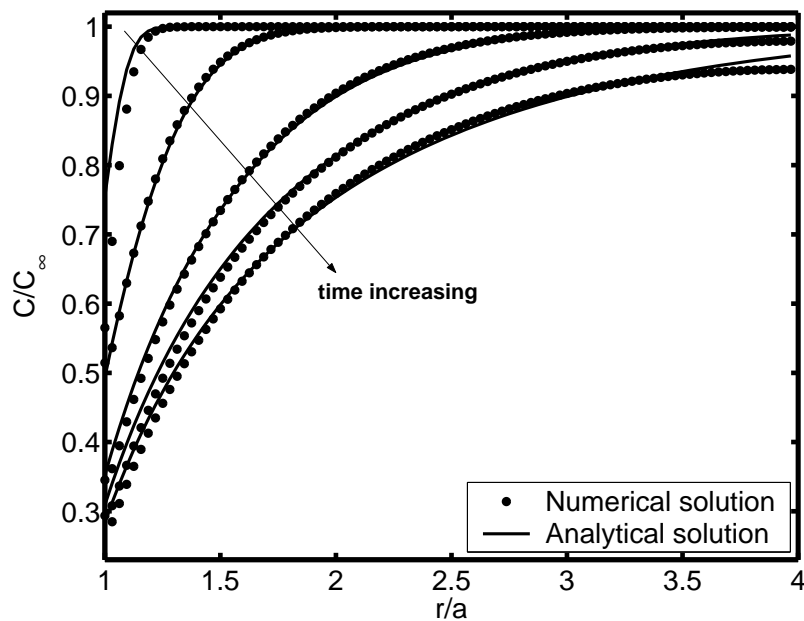
Figure 3.12: Diffusion test for the bulk surfactant concentration. Bulk surfactant concentration profiles at $t^* = 0.0037, 0.0637, 0.4875, 1.3312$ and 3.1125 .
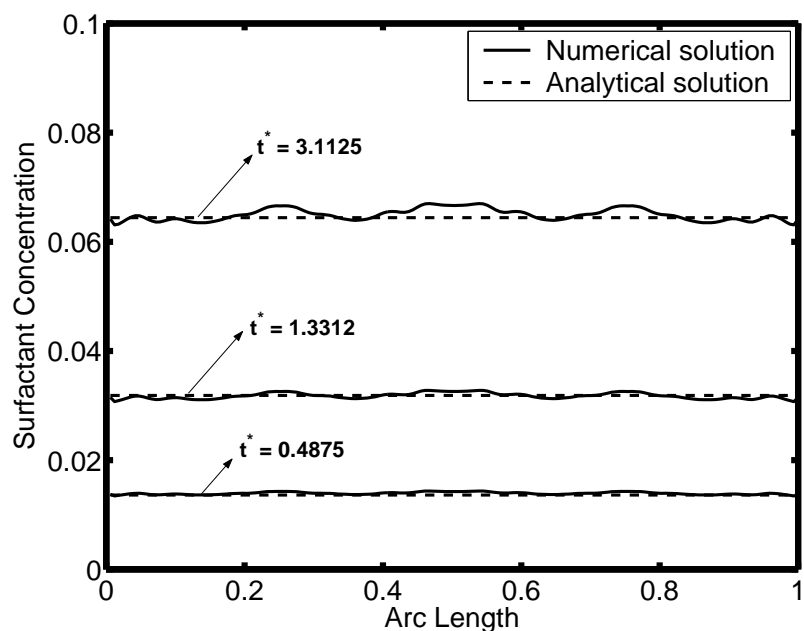
Figure 3.13: Diffusion test for the bulk surfactant concentration. Drop interface surfactant concentration profiles at $t^* = 0.4875, 1.3312$ and 3.1125 .
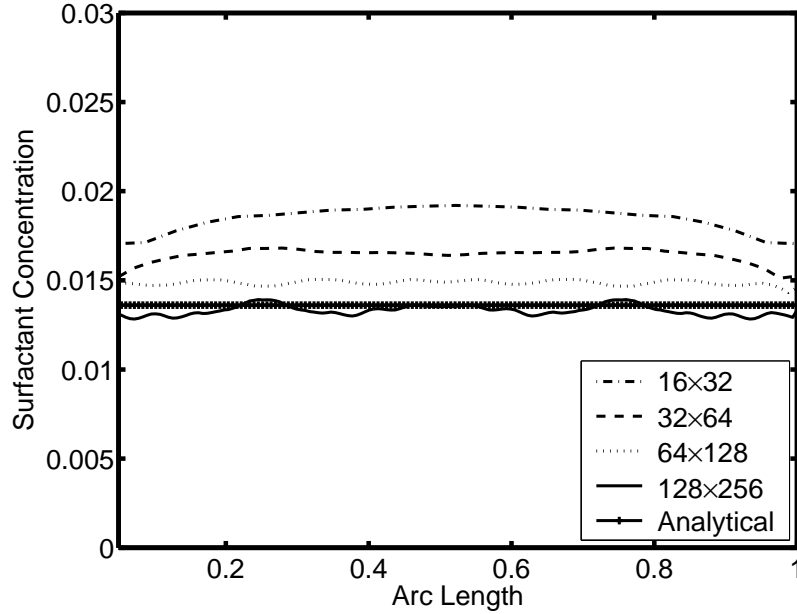
Figure 3.14: Convergence test for surface concentration with adsorption for a stationary drop in a tube. Drop interface surfactant concentration profiles for various grid resolutions at $t^* = 0.4875$.

3.5 Marangoni Effect Test

In order to investigate the Marangoni effect, a simple test case proposed by by Zhang et al. [42], is performed. In this test case, an initially spherical drop is considered with a nonuniformly distributed surfactant concentration Γ given by

$$\Gamma = \Gamma_o \left(1 + \tanh(4(\frac{\theta}{\pi} - 0.5)) \right). \tag{3.14}$$

Due to the nonuniform distribution of surfactant over the interface, surface tension σ is also distributed nonuniformly and depending on the surfactant concentration by the nonlinear equation of state, i.e., Langmuir equation of state given by

$$\sigma = \max \left(\sigma_{min}, \sigma_s[1 + E(\ln(1 - \frac{\Gamma}{\Gamma_\infty})] \right), \tag{3.15}$$

where σ_{min} is the minimum surface tension value, σ_s is the surface tension for the clean interface, E is the elasticity number given by $E = \frac{RT\Gamma_\infty}{\sigma_s}$ and Γ_∞ is the maximum surfactant concentration for the surfactant, respectively. The first term at the right hand side of

Eq. (3.15) represents the contribution of the initial surface tension and the second term represents the contribution of the variation of surfactant concentration.

Initially, bubble and the bulk phase are quiescent. There is no surfactant transfer from bulk fluid to the bubble surface, i.e., source term is turned off, and all diffusive terms are neglected. Because of the variation of the surface tension along the interface, there is a Marangoni effect which causes a flow away from regions of low surface tension. In computations, parameters are chosen same as those of Zhang et al. [42] used, i.e., $R = 0.01$ m, $L = 0.03$ m, $a = 0.005$ m, $\rho_1 = 1000$ kg/m^3, $\rho_2 = 100$ kg/m^3, $\mu_1 = 0.01$ Ns/m^2 and $\mu_2 = 0.001$ Ns/m^2 where the indices 1 and 2 represents the bulk fluid and the drop, respectively. Also, we let $\sigma_s = 2.5 \times 10^{-6}$ N/m and $E = 0.1$, which are not stated exactly in the study of Zhang et al. [42]. Computational domain is resolved by a uniform Cartesian grid containing 16×48 grid cells.

Initially, surface concentration is maximum at the bottom of the drop, $(s = 0)$, and zero at the top of the drop, $(s = 1)$ where s is the dimensionless arc length. Due to this fact, a gradient is created which causes a Marangoni flow along the interface. As can be seen in Fig. 3.15, this Marangoni flow sweeps the surfactant towards the upper part of the drop and surfactant concentration at the bottom part dilutes as the time evolves. The velocity field of the drop and the surrounding fluid is shown in Fig. 3.16. Moreover, Marangoni effect initiates the propulsion of the drop which causes the drop to move from its initial position as shown in Fig. 3.17.
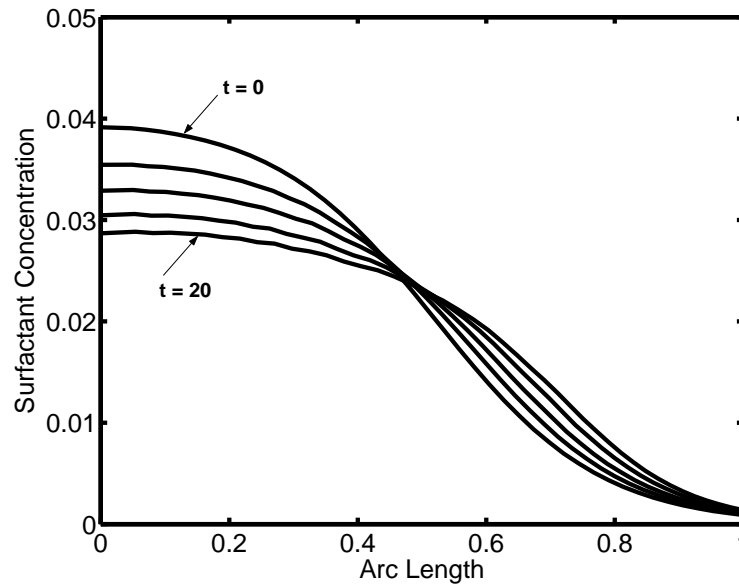
Figure 3.15: Evolution of the surfactant concentration over a bubble surface having an initial nonuniform surfactant distribution at $t = 0, 5, 10, 15$ and 20.
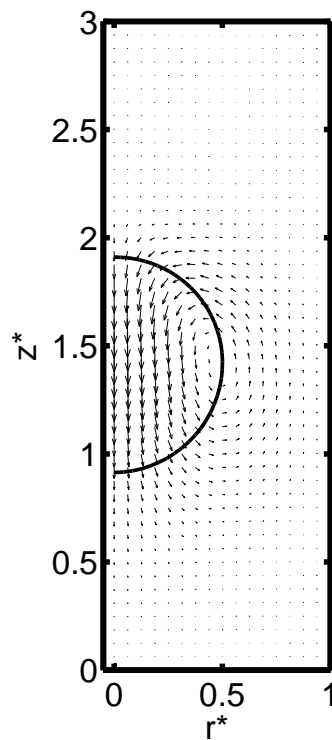
Figure 3.16: Marangoni effect for an initially nonuniform surfactant covered bubble in a tube. Velocity field for the bubble at $t = 20$.
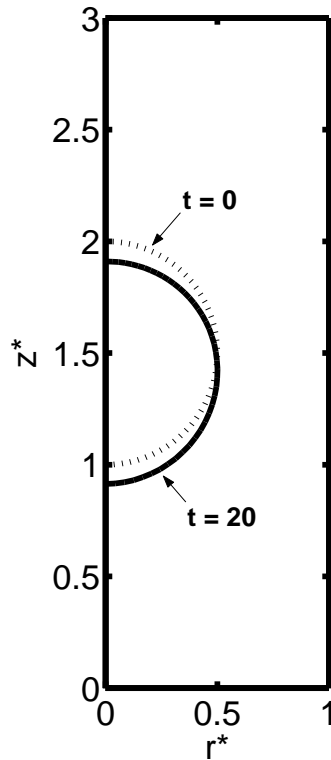
Figure 3.17: Marangoni effect for an initially nonuniform surfactant covered bubble in a tube. Bubble locations at $t = 0$ (dotted line) and $t = 20$ (solid line).

Although a qualitative correspondence is found when compared with the study of Zhang et al. [42], there is a slight difference between the surfactant concentration profiles at the midway between the top and the bottom of the drop. This difference may arise from the estimation of some parameter values, such as elasticity number or Reynolds number. However our results are qualitatively in good agreement with their conclusions.

Chapter 4

CLEAVAGE OF A VISCOUS DROP BY SURFACTANT

After validating the numerical solution algorithm for simple test cases in the previous chapter, the method is now applied to study the cleavage of a viscous drop by surfactant - a problem studied by Greenspan [10, 11] experimentally as a model for cytokinesis. The problem was recently studied computationally by He and Dembo [17, 18]. This problem is studied here using the present FD/FT method. This chapter begins with the description of the problem including the overview of Greenspan's oil droplet experiment and the computational setup of the problem. Finally, in Section 4.2, grid convergence of the method is examined and the results including the numerical simulations of the deformation of a viscous droplet under the influence of a surface tension gradient generated by the release of surfactant at the poles are presented and discussed.

4.1 Description of the Problem

4.1.1 Experimental Setup

As discussed in the Introduction, Greenspan [10, 11] proposed a model for the cytokinesis of biological cells and showed that an oil droplet under the action of a surfactant can undergo a considerable deformation leading, in the extreme case, to entire cleavage. There is a very noticeable similarity in the images of droplets during the final stages of cleavage and images of cytokinesis [14].

In the Greenspan's experiment, as sketched in Fig. 4.1, controlled amount of the surface active material NaOH (sodium hydroxide), was released symmetrically at the opposite poles of an oil droplet which is neutrally buoyant in the surrounding solvent, i.e. weakly stratified salt water solution. A wide range of oil blends were tested, however, large deformations by the effect of surfactant were achieved in only two blends. These blends were the 2:1 mixture of cod liver/olive and the 2:1 mixture of Gulf SAE90 (gear case lubricant)/rapeseed. The nonuniform distribution of the surfactant causes saponification of fatty acid asters and the

diffusion and the convection of the reaction products results in a nonuniform surface tension distribution; high at the equator and low at the poles.
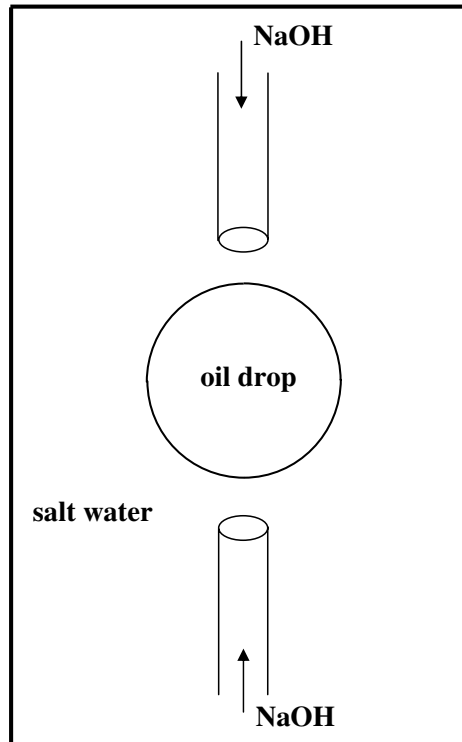
Figure 4.1: A schematic representation of the Greenspan's oil droplet experiment.

When the surfactant was released as a short burst, droplet deformed quickly in the axial direction within one or two seconds, where the relaxation back to the original shape was slow. In the case of the first blend, the reduction in the equatorial diameter was approximately %50 and the droplet recovers its spherical shape when the supply of the surfactant was removed. In the case of the second blend, deformations were larger and very deep furrowing was observed ending with a narrow bridge connecting the two daughter droplets which are almost spherical. This final bridge appeared to have some stability but it was fragile and can be ruptured by external effects or in some cases, it ruptured itself leading to a complete division. Also, the last stage of cytokinesis involves a similar narrow bridge between daughter cells which persists for a long time [13].

4.1.2   Computational Setup

In order to simulate the Greenspan's oil droplet experiment, as sketched in Fig. 4.2, an initially clean droplet of radius a is placed at the center of a cylindirical tube and on the axis of symmetry represented by black dashed dot line extending three drop radius in the radial direction, $L = 3a$, and nine drop radius in the axial direction, $H = 9a$. Bulk surfactant is introduced continuously at the north and south poles of the droplet uniformly in a band extending Ωa in the radial direction where Ω is taken 0.95 in the present computations unless specified otherwise. The results are presented in terms of nondimensional quantitites. For this purpose, $L = a$, $\mathcal{T} = \frac{\mu a}{\sigma_s}$ and $\mathcal{V} = \frac{\sigma_s}{\mu}$ are used as the length, time and velocity scales, respectively. The computations are performed using a 128×384 uniform grid.
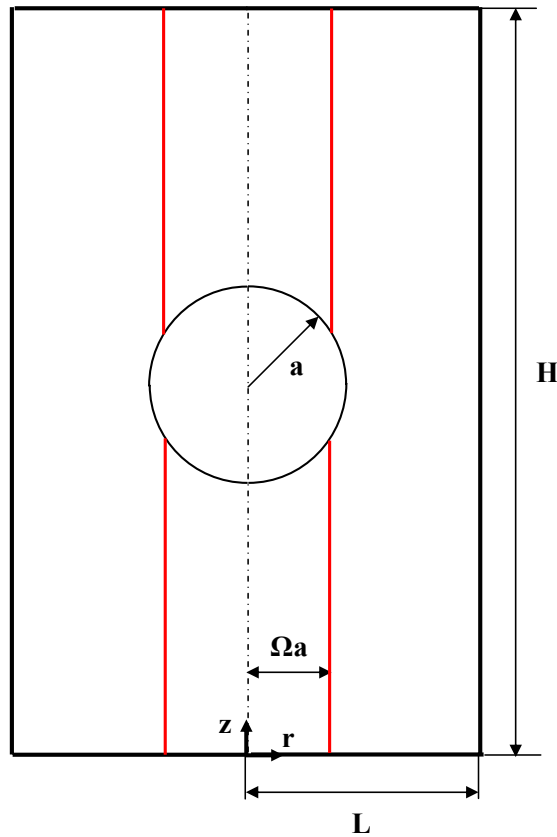

Figure 4.2: A schematic representation of the computational setup used in the simulation of Greenspan's oil droplet experiment.

4.2 Results and Discussion

In order to determine the reference case for the whole computations, a case which leads to a clean breakup is investigated. For this purpose, a wide range of parameters including the surface Peclet number (Pe_s), the bulk Peclet number (Pe_c), the Damkohler number (Da), the Biot number (Bi), the elasticity number (E) and the adsorption number (k) are considered and a clean breakup is achieved for the parameters $Pe_s = 2000$, $Pe_c = 500$, $Da = 0.0001$, $Bi = 15.0$, $E = 0.95$ and $k = 5.0$. For this case, the drop cleavage process is illustrated in Fig. 4.3 where the snapshots of the drop interface and the bulk surfactant concentration contours are plotted at various time frames. The density and viscosity ratios are set to unity and two, respectively. Also, the surfactant concentration profiles at the drop interface is shown in Fig. 4.4 where the arc length is defined in the clockwise direction starting from the top and is normalized by the initial perimeter of the drop. As can be seen in Figs. 4.3 and 4.4, the surfactant concentration increases at the interface near the north and south poles of the drop initially, then is kept on a constant value at these regions because of the continuous supply of the surfactant at both ends of the drop. Accumulation of surfactant at the drop poles and the surface diffusion reduces the surface tension at the poles and causes the drop elongate in the axial direction leading the breakup of the drop into two large and one small (satallite) droplets. However small droplets are deleted in order to avoid the resolution problem in the current implementation. The symmetry and smoothness of the bulk surfactant contours in Fig. 4.3 may be considered as an indication for the accuracy of computations. These drop shapes qualitatively compare well with the oil droplet shapes observed by Greenpsan [10]. The drop interface along with the velocity field in the vicinity of the drop is plotted in Fig. 4.5. Note that the velocity vectors are shown on every three grid points to obtain a better view. As can be seen in this figure, there are two stagnation points located very close to the north and south poles of the drop. Because the surface flow advects the surfactant towards the stagnation points, the maximum surfactant concentration at the interface is expected to locate at these points corresponding to $s = 0.17$ and $s = 1.55$ which can be obtained from Fig. 4.4 for $t^* = 237.5$. However this claim is not quantified here. Also, the case where the bulk surfactant concentration is applied instantaneously at the north and south poles of the drop is simulated. As it is seen in Fig. 4.6, breakup mechanism of the drop differs significantly from the case with the continuous supply of surfactant. Here,

necking occurs in two regions where the daughter droplets do not preserve their spherical shape. Surfactant concentration profiles at the interface is shown in Fig. 4.7 for this case. As can be seen in this figure, surfactant concentration reduces at the poles of the drop as time progresses and tends to distribute uniformly. Finally, in Fig. 4.8, the grid convergence of the method is shown for the case where the bulk surfactant is supplied continuously to the poles of the drop. Here, deformation is plotted for various grid resolutions between 32×96 and 128×384. The deformation is defined as

$$D_L = \frac{L - a}{a}, \tag{4.1}$$

where L is the half-length of the drop at the axial direction and a is the initial radius of the drop. The deformation of the drop increases up to a limiting value at which the drop breaks up. As can be seen in Fig. 4.8, the differences between deformations computed on successive grids reduce as the grid is refined indicating the grid convergence of the method. Note that, the case where the bulk surfactant is supplied continuously at the poles of the drop is considered for the grid convergence test.

4.2.1 The Influence of the Surface Peclet Number

In this section, the results from a systematic investigation varying the surface Peclet number Pe_s for fixed values of the rest of the parameters are presented. All numerical simulations were started with a clean interface, i.e., no surfactant at the drop interface initially ($\Gamma(0, s) = 0$). With the onset of the surfactant supply from the north and south poles of the viscous drop, surfactant molecules diffuse on the interface and set up a nonuniform concentration distribution along the interface. In general, we expect that the evolution of surfactant concentration and drop shape will be different for different surface diffusivity. Deformation is plotted as a function of time for various surface Peclet numbers between $Pe_s = 1.0$ and $Pe_s = 10.0$ in Fig. 4.9, continued until the breakup of the drop. The rest of the parameters are the same as before. Unlike in the former case, deformation is defined here via the evolution of the surface area of the drop in time in order to show the entire deformation and given by

$$D_A = \frac{A - A_0}{A_0}, \tag{4.2}$$

Figure 4.3: Cleavage of a viscous drop by surfactant. The drop interface is plotted together with the bulk surfactant concentration contours at time frames $t^* = 0$, 19.8, 74.9, 150.1, 187.5, 237.5, 287.5, 450 and 500. Time progress from left to right and top to bottom. The bulk concentration is kept constant at the poles to simulate continuous supply of surfactant. Grid: 128×384.

Figure 4.4: Cleavage of a viscous drop by surfactant. The surfactant concentration at the drop interface is plotted against normalized arc length. The bulk concentration is kept constant at the poles to simulate continuous supply of surfactant.
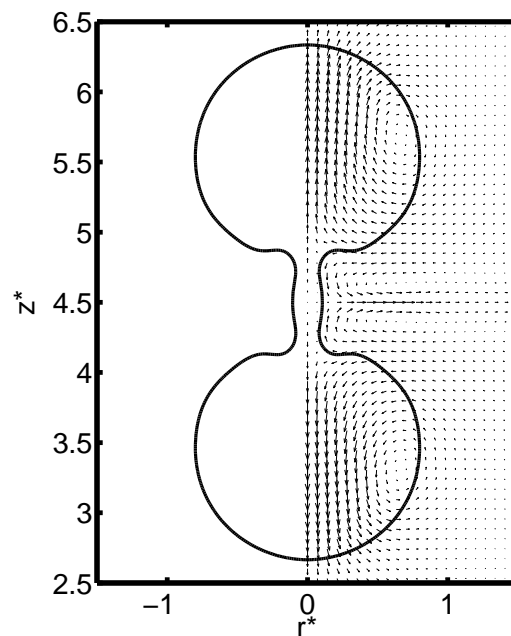
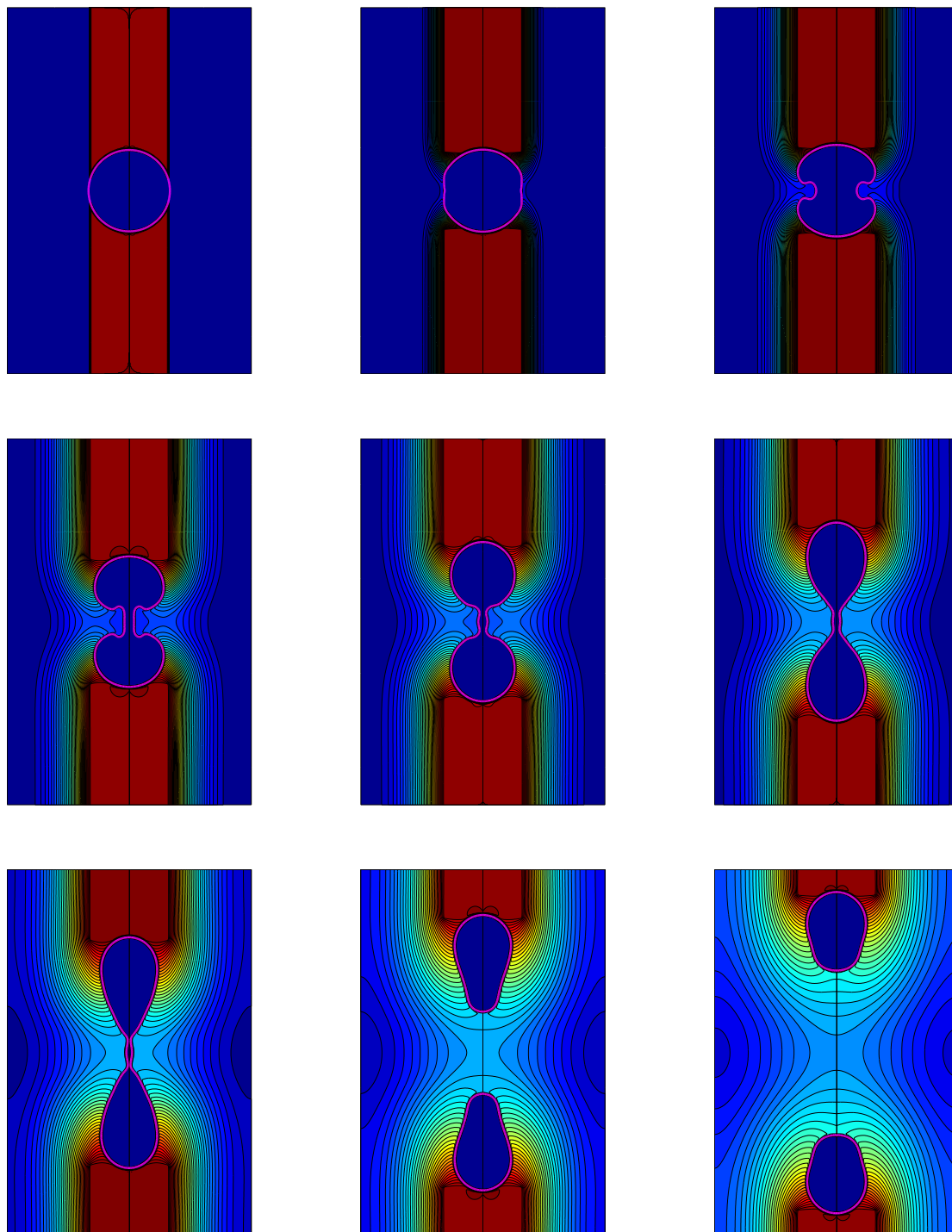Figure 4.5: Velocity vectors in the vicinity of the drop. Grid : 128×384, $t^* = 237.5$.
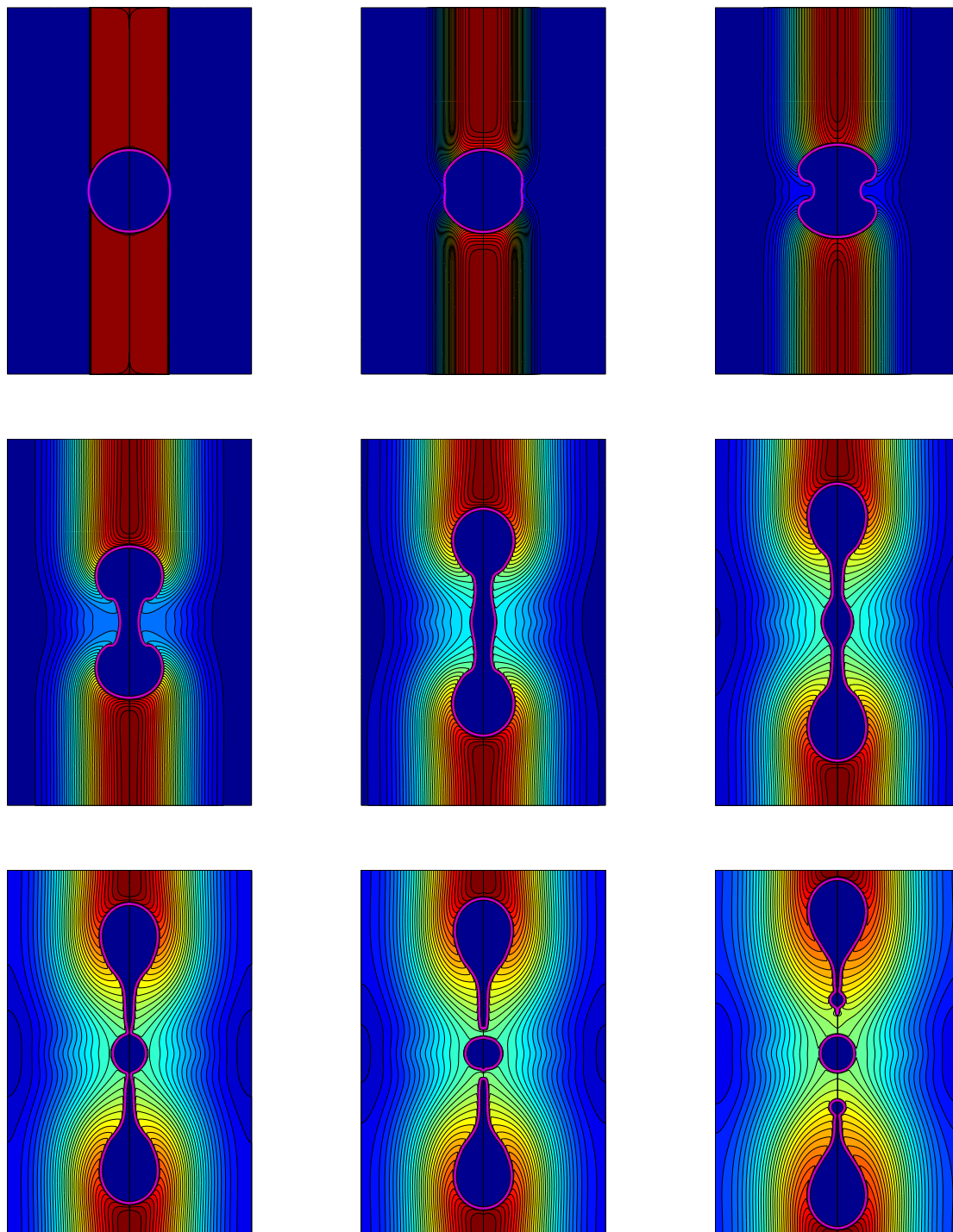
Figure 4.6: Cleavage of a viscous drop by surfactant. The drop interface is plotted together with the bulk surfactant concentration contours at time frames $t^* = 0$, 19.8, 74.9, 150.1, 187.5, 237.5, 287.5, 450 and 500. Time progress from left to right and top to bottom. The bulk concentration is applied instantaneously at the poles of the drop. Grid: 128×384.
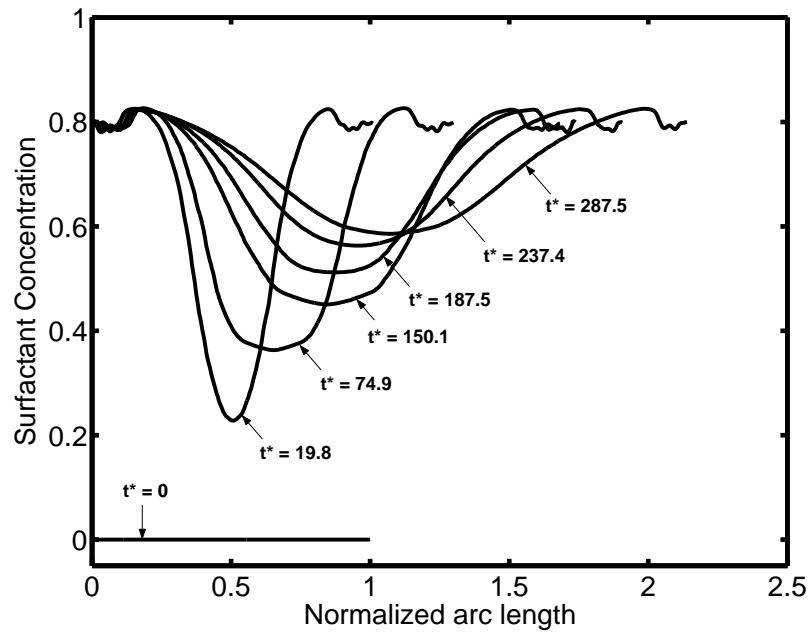
Figure 4.7: Cleavage of a viscous drop by surfactant. The surfactant concentration at the drop interface is plotted against normalized arc length. The bulk concentration is applied instantaneously at the poles of the drop.

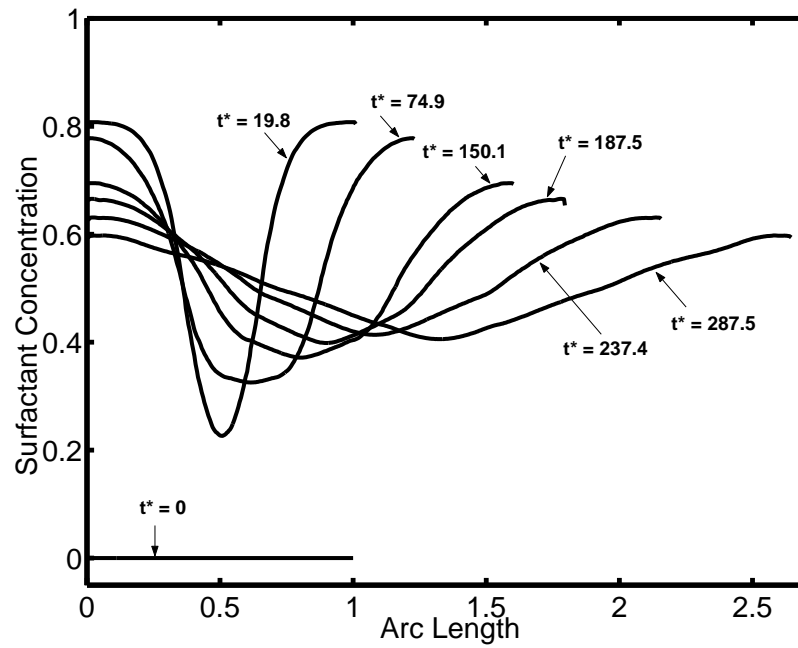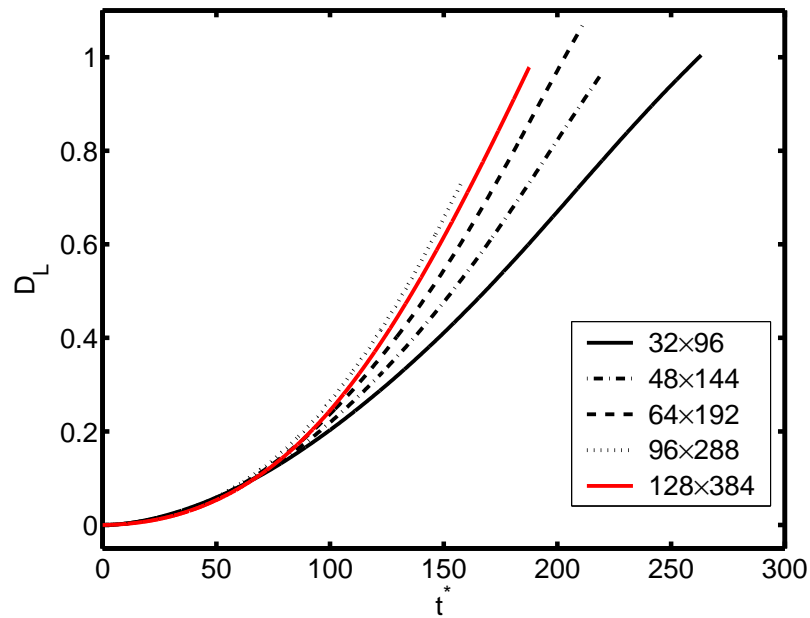Figure 4.8: Deformation versus nondimensional time using various grid resolutions.

where A and A_0 are the surface area of the drop at the current and initial time frames, respectively. As can be seen in this figure, drop cleavage occurs for $Pe_s \geq 3.0$ but not for the values below where the drop oscillates and eventually relaxes to its initial spherical shape. For small values of Pe_s, surface convection of surfactant is weak compared to the surface diffusion, so that the surface diffusivity quickly homogenizes the surfactant concentration at the drop interface before the drop breaks up. In Fig. 4.10, snapshots of drops taken at various times for $Pe_s = 1.0$ and $Pe_s = 4.0$. As can be seen in these snapshots, the drop deforms in a damped oscillatory motion and eventually relaxes back to a spherical shape in the case of $Pe_s = 1.0$, while the drop tends to go into a complete cleavage for $Pe_s = 4.0$.

Figure 4.11 shows the surfactant concentration profiles for different Pe_s at a fixed time. As Pe_s increases, surface diffusivity weakens and the surfactant distribution on the drop interface is controlled by the surface convection producing large variations in surfactant distribution leading to large deformations. Also, drop shape profiles are shown in Fig. 4.12. As can be seen in this figure, drop with less diffusivity elongates more in the axial direction demonstrating large surface tension gradients which tend to deform the drop more. Note that we have performed simulations for various surface Peclet numbers ranging between $Pe_s = 0.1$ and $Pe_s = 8000$, however, only the current results are shown due to space considerations. For high Pe_s, deformations and surfactant concentration profiles are very close to each other so they are not shown here. For low Pe_s, the drop continues to deform in a damped oscillatory motion, however, the amplitude of the oscillations decreases as Pe_s decreases. The latter condition arises from the quick homogenization of the surfactant at the drop interface due to diffusion.
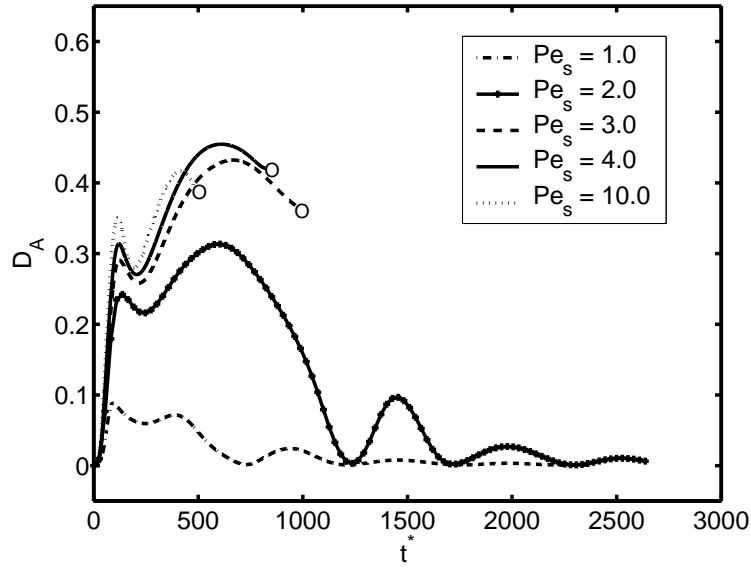
Figure 4.9: Deformation versus nondimensional time for $Pe_s = 1.0$, $Pe_s = 2.0$, $Pe_s = 3.0$, $Pe_s = 4.0$ and $Pe_s = 10.0$. The drop breaks up for $Pe_s = 3.0$ and above while it oscillates and relaxes back to its initial spherical shape for $Pe_s = 2.0$ and below. ◯ denotes drop breakup.
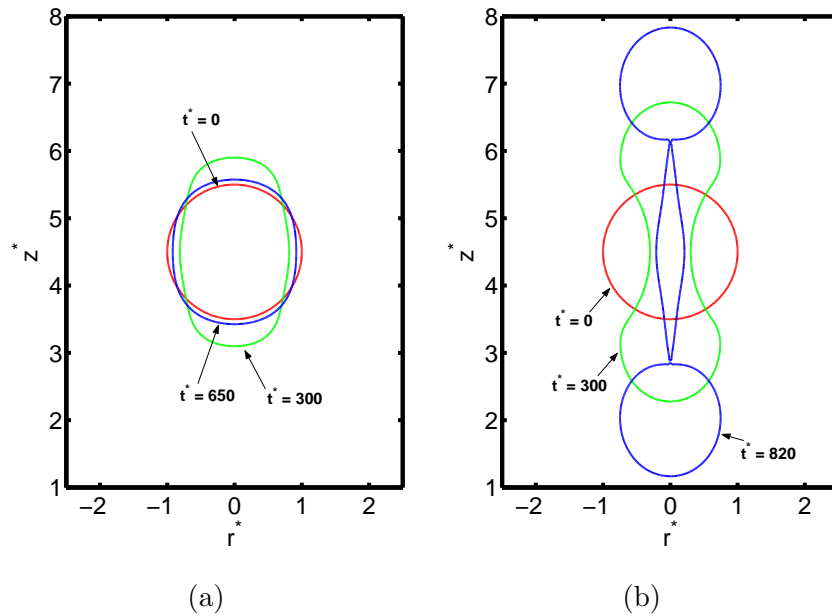
Figure 4.10: Cleavage of a viscous drop by surfactant. The drop interface is plotted for $Pe_s = 1.0$ and $Pe_s = 4.0$ at various time frames. On the left, the drop oscillates and relaxes back to its initial spherical shape for $Pe_s = 1.0$ while, on the right, it breaks up for $Pe_s = 4.0$.
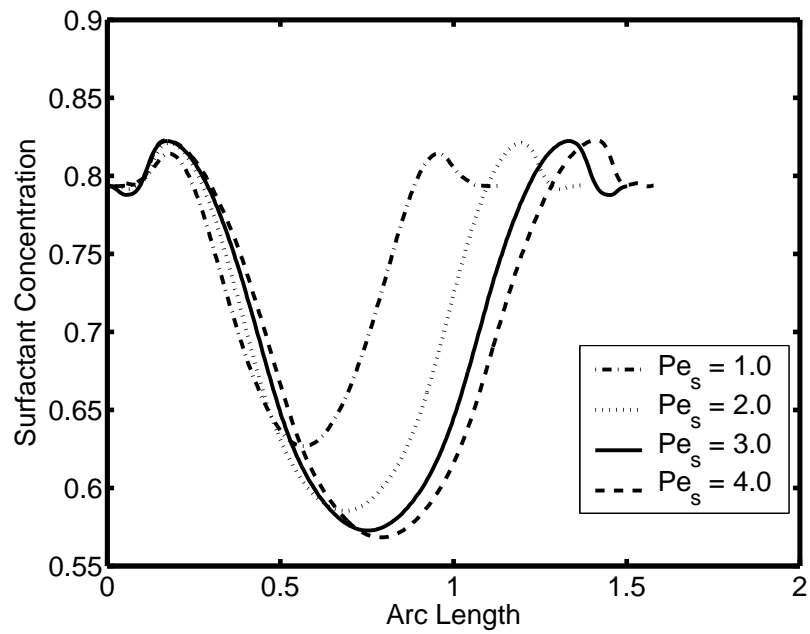
Figure 4.11: Surfactant concentration profiles at the drop interface for $Pe_s = 1.0$, $Pe_s = 2.0$, $Pe_s = 3.0$ and $Pe_s = 4.0$ at $t^* = 247.5$.
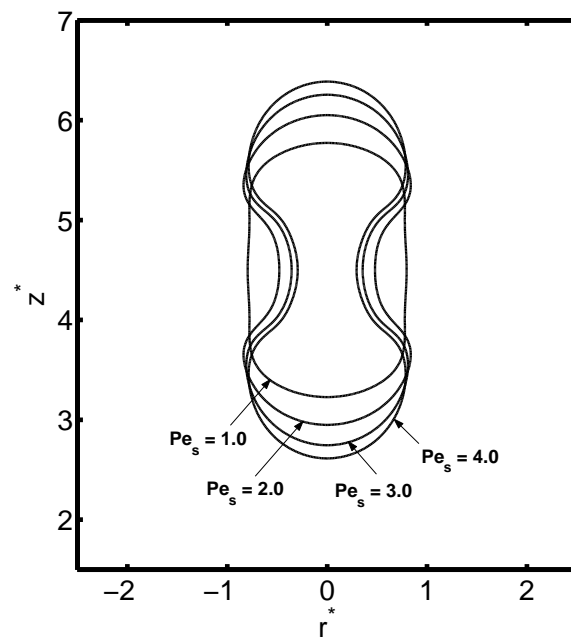
Figure 4.12: Drop interface profiles for $Pe_s = 1.0$, $Pe_s = 2.0$, $Pe_s = 3.0$ and $Pe_s = 4.0$ at $t^* = 247.5$.

4.2.2   The Influence of the Damkohler Number

The dimensionless parameter that governs the transport of surfactant at the bulk phase is the Damkohler number Da, i.e., the ratio of the adsorptive and bulk diffusive fluxes. In general, as the Damkohler number is increased, adsorption-desorption process is enhanced relative to the bulk diffusion and the mass transfer from bulk to the interface is controlled by diffusion. The influence of the Damkohler number on drop deformation is examined in Fig. 4.13. As can be seen in this figure, when $Da = 10^{-3}$, drop acts to restore its initial spherical shape and does not break up. On the other hand, for $Da = 10^{-4}$ and $Da = 10^{-5}$, deformations are much larger and drop eventually breaks up. Although not shown here, drop deformations for the values of $Da > 10^{-3}$ preserves its oscillatory character, while for the values of $Da < 10^{-3}$, drop deformation profiles are very close to each other and break up occurs for all cases in this range. Also, bulk surfactant concentration profiles for $Da = 10^{-3}$ and $Da = 10^{-4}$ in Fig. 4.14, where the dominant character of the diffusion process at the bulk can be clearly seen for the higher value of the Damkohler number, i.e., $Da = 10^{-3}$.
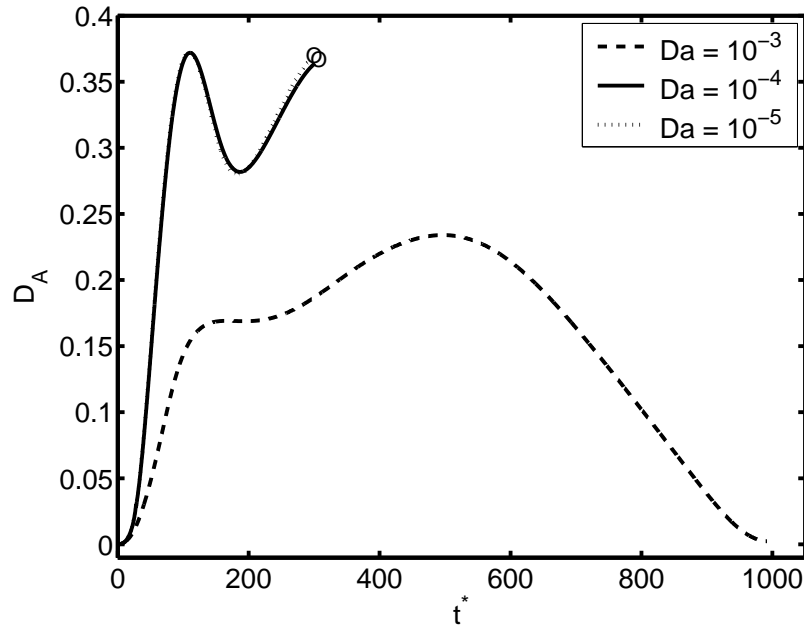
Figure 4.13: Deformation versus nondimensional time for $Da = 10^{-3}$, $Da = 10^{-4}$ and $Da = 10^{-5}$. The drop breaks up for $Da = 10^{-4}$ and $Da = 10^{-5}$, while it acts to preserve its initial spherical shape for $Da = 10^{-3}$. $\bigcirc$ denotes drop breakup.
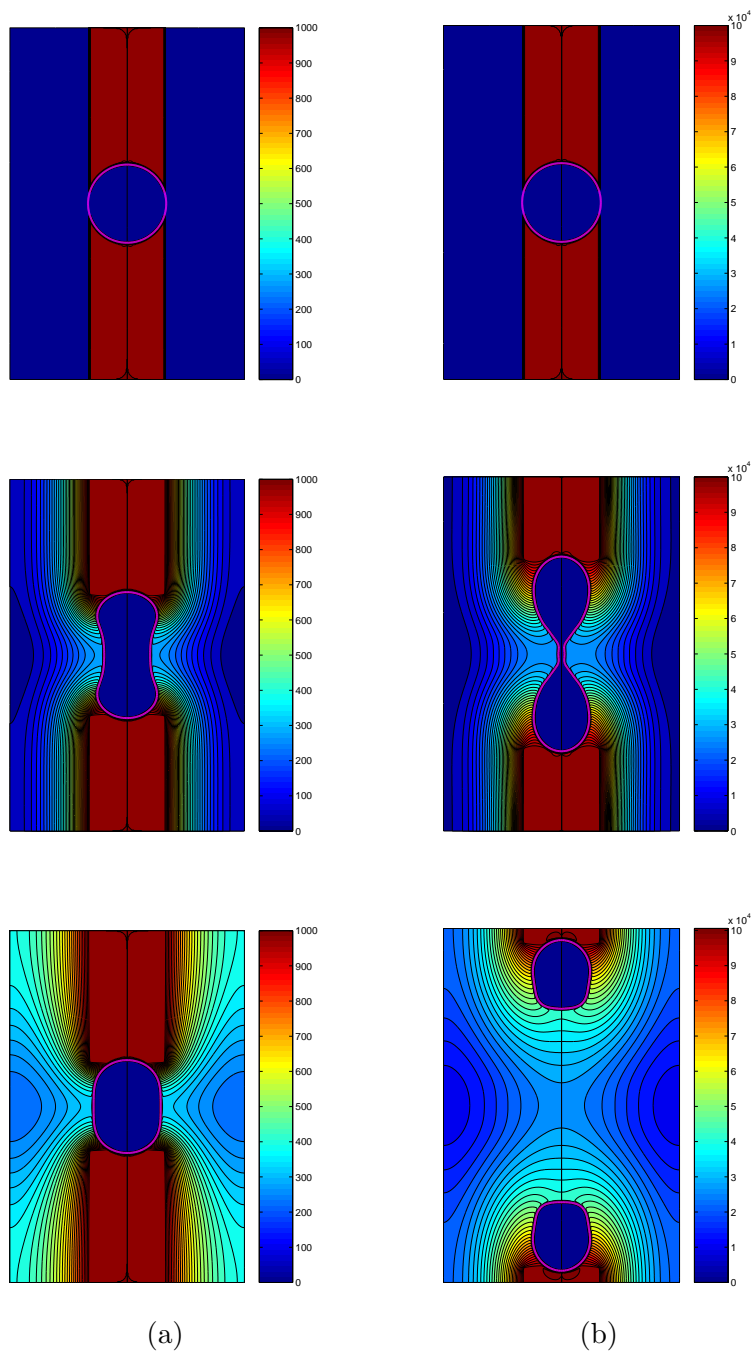
Figure 4.14: Cleavage of a viscous drop by surfactant. The drop interface is plotted together with the bulk surfactant concentration contours at time frames $t^* = 0$, 237.5 abd 850. Time progress from top to bottom. (a) $Da = 10^{-3}$, (b) $Da = 10^{-4}$.

4.2.3 The Influence of the Adsorption Number

The adsorption number k is the ratio of characteristic adsorption and desorption rates. As discussed in Section 3.4, mass transfer from bulk phase to the drop interface is achieved by an adsorption-desorption mechanism where the surfactant is soluble in the bulk phase. In general, as the adsorption number increases, more surfactant is expected to be transferred onto the interface resulting in more severe surface tension gradients along the interface which may cause the drop breaks up eventually. This behaviour can be clearly seen in Fig. 4.15 where the drop deformation is plotted against the nondimensional time for various adsorption numbers. For the lower values of k, i.e., $k = 0.1$, $k = 0.5$ and $k = 0.7$, the general trend of the drop deformation looks like damped oscillatory motion, while for the values of the adsorption number, $k > 0.7$, drop breakup is observed. The oscillatory character of the drop deformation for $k = 0.5$ and the cleavage of the drop for $k = 5.0$ are shown in Fig. 4.16 where the drop interface is plotted at various time frames. As it is seen in Fig. 4.16a, for $k = 0.5$ drop tends to recover its initial spherical shape, while for $k = 5.0$ drop tends to go into a breakup. Also, surfactant concentration profiles at the drop interface is shown in Fig. 4.17. As can be seen in this figure, as the adsorption number is increased, surfactant concentrations become higher as well as the surfactant distribution profiles at the drop interface is more nonuniform causing large surface tension gradients. This difference in the surfactant concentration distribution affects the drop breakup mechanisms significantly. Figure 4.18 shows the evolution of the drop shapes until the breakup is observed for $k = 0.8$, i.e., drop A, and $k = 5.0$, i.e., drop B. For drop A, surfactant is distributed more uniformly compared to drop B causing drop A to elongate more in the axial direction just before the breakup. It is interesting to note that the necking occurs in both upper and lower sides of drop A and the breakup is achieved from these points to give three daughter droplets. In the current simulations, all parameters except the adsorption number are taken the same as before.
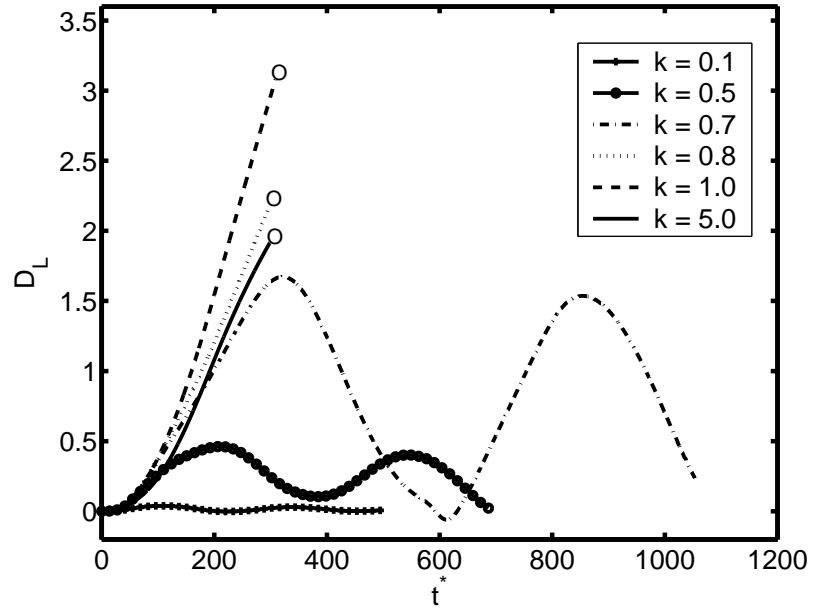
Figure 4.15: Deformation versus nondimensional time for various adsorption numbers. The drop breaks up for $k = 0.8$, $k = 1.0$ and $k = 5.0$, while it acts to preserve its initial spherical shape for $k = 0.1$, $k = 0.5$ and $k = 0.7$. $\bigcirc$ denotes drop breakup.

(a)

(b)
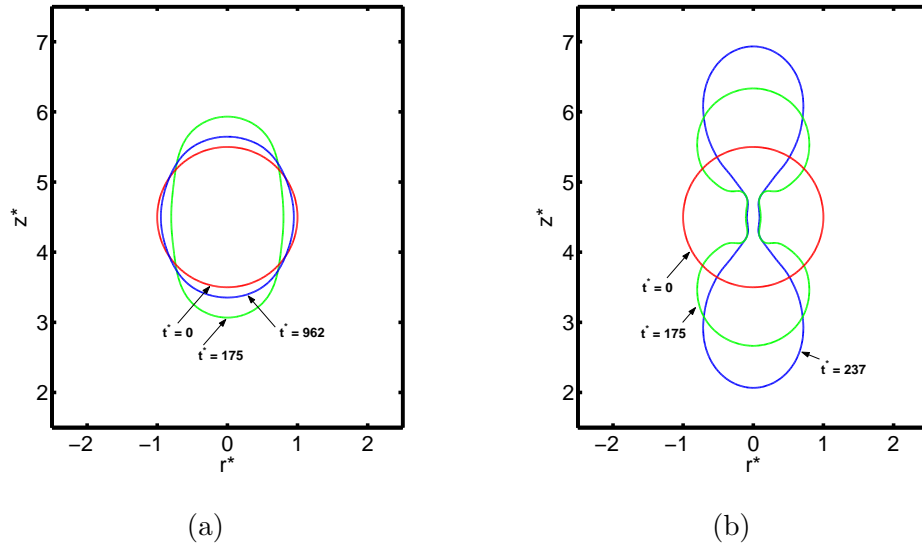
Figure 4.16: Cleavage of a viscous drop by surfactant. The drop interface is plotted for $k = 0.5$ and $k = 5.0$ at various time frames. On the left, the drop oscillates and relaxes back to its initial spherical shape for $k = 0.5$ while, on the right, it breaks up for $k = 5.0$.
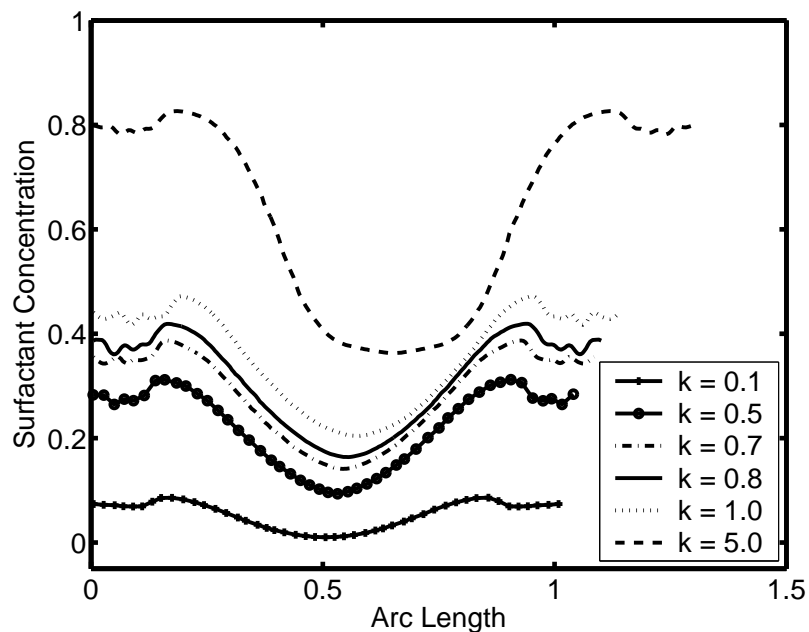
Figure 4.17: Surfactant concentration versus normalized arc length for various adsorption numbers at $t^* = 237.5$.
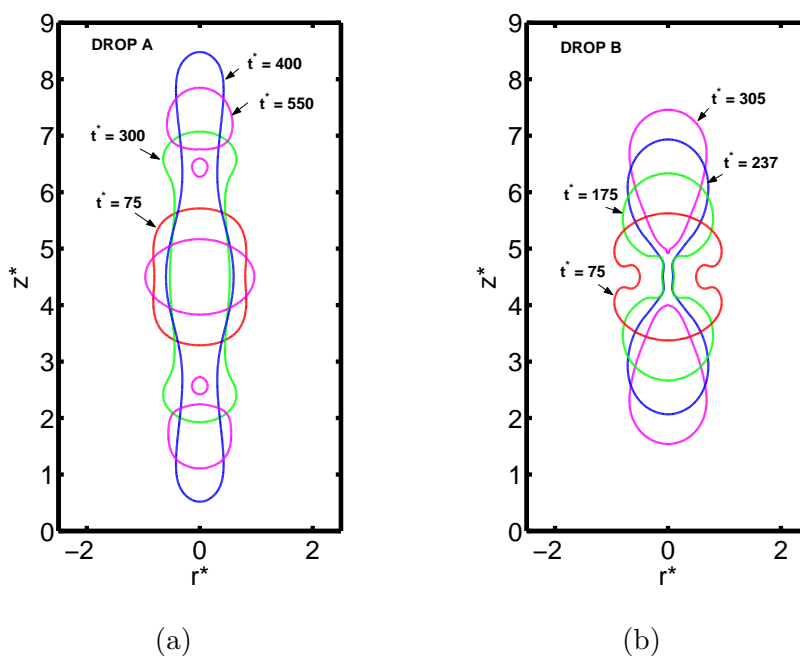
Figure 4.18: Drop breakup mechanisms at different adsorption numbers. The drop interface is plotted for $k = 0.8$, i.e., drop A, and $k = 5.0$, i.e., drop B at various time frames.

4.2.4 The Influence of the Biot Number

The dimensionless parameter that governs the interfacial adsorption-desorption of surfactant is the Biot number Bi, i.e., the ratio of the characteristic sorption rate to the interfacial convection of surfactant. In general, as the Biot number increases, the adsorption rate relative to the surface convection becomes faster than the ratio of desorption rate to the surface convection. In other words, surfactant supply to the poles of the drop is faster than the removal of the surfactant from the drop interface. Therefore, large deformations are expected for the high Biot numbers relative to low Biot numbers. In Fig. 4.19, drop deformations are shown for different Biot numbers. As can be seen in this figure, for the relatively small Biot numbers, drop deformations are very small and breakup is not observed. At relatively high Biot numbers, deformation increases, even results in a breakup. Although a wide range of parameter values for Bi is considered, only the results for $Bi = 0.01$, $Bi = 0.1$, $Bi = 1.0$ and $Bi = 10.0$ are presented here.

Figure 4.19: Deformation versus time for $Bi = 0.01$, $Bi = 0.1$, $Bi = 1.0$ and $Bi = 10.0$. The drop breaks up for $Bi = 1.0$ and above while it oscillates and relaxes back to its initial spherical shape for $Bi = 0.1$ and below. ◯ denotes drop breakup.

Chapter 5

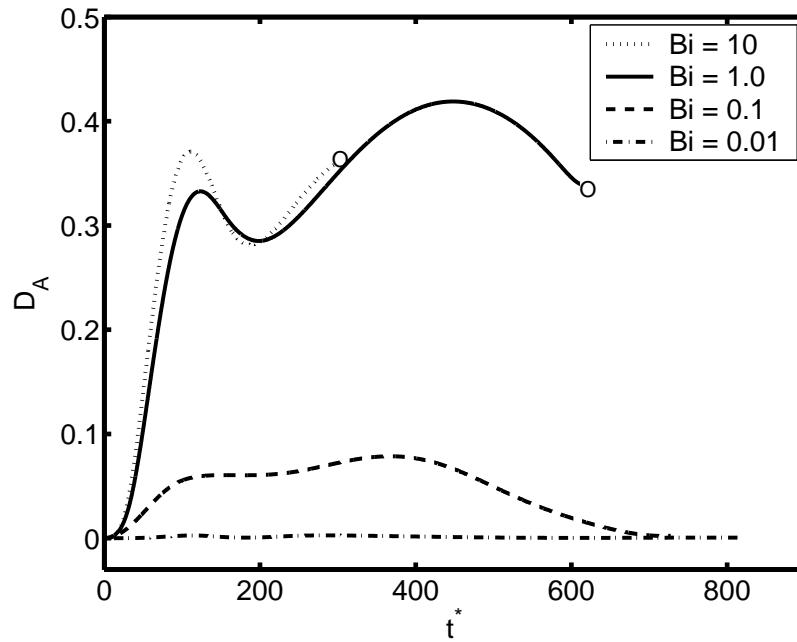# CONCLUSIONS

A general computational procedure is developed here based on the finite-difference/front-tracking (FD/FT) method [34] for simulations of interfacial flows with soluble surfactants. The governing equations for axisymmetric geometry are solved numerically on a fixed, regular, staggered grid while the drop interface is represented by a Lagrangian grid with connected marker points. Convection/diffusion equations for surfactant at the interface and in the bulk fluid are solved fully coupled with the flow equations. The method can employ virtually any nonlinear equation of state that relates interfacial tension to the surfactant concentration at the interface.

The numerical algorithm is validated using several simple test cases for which analytical solutions are available. First, a simple test case of a continuosly expanding drop interface without the effects of the surface diffusion and source terms is considered to validate the numerical approximation to the convective terms in the surfactant transport equation at the interface. The numerical results are found in an excellent agreement with the analytical solution indicating the accurate discretization of the convective terms in surfactant evolution equation. Secondly, diffusive terms in the surfactant transport equation at the interface are tested. For this purpose, the flow field and the source terms are turned off and let the surfactant evolution be only due to the diffusion on the interface initially covered by a nonuniformly distributed surfactant. The solutions for the various surface diffusivities match very well with the analytical solutions for this test case. Thirdly, source term is tested by considering the mass transfer from bulk to interface solely due to the adsorption-desorption process. In this test case, the diffusive and convective terms are neglected and the bulk surfactant is considered insoluble. Numerical and analytical solutions are compared for different Biot numbers, i.e., different mass transfer rates. The numerical solutions converge to the analytical solutions for relatively low Biot numbers where the time-stepping error is small. Then, bulk surfactant diffusion and the mass transfer between the bulk and the

drop interface is tested by considering a soluble surfactant in the bulk phase. Numerical solutions also match very well with the analytical solutions for the evolution of surfactant concentration in both bulk phase and the drop interface. The final test case deals with the Marangoni effect which is proposed by Zhang et al. [42]. Although it is not possible to make a quantitative comparison between the results because of the estimation of some parameter values, the results are found to be qualitatively in a good agreement with their conclusions.

Then the method is applied to study the cleavage of a viscous drop by surfactant - a problem studied by Greenspan [10, 11] experimentally as a model for cytokinesis. First a wide range of parameters including the surface Peclet number (Pe_s), the bulk Peclet number (Pe_c), the Damkohler number (Da), the Biot number (Bi), the elasticity number (E) and the adsorption number (k) are considered to achieve a clean breakup. After determining the reference case where the bulk surfactant is applied continuously from the drop poles, it is compared with the case where the bulk surfactant is applied instantaneously from the drop poles. It is found that the evolution of the drop shapes in the first case compare well with the oil droplet shapes observed by Greenpsan [10]. Then the effects of the surface Peclet number, the Damkohler number, the adsorption number and the Biot number are investigated on the deformation and breakup of the drop individually. It is found that for the different surface diffusivities, bulk diffusivities and mass transfer regimes, drop undergoes large deformations even resulted with breakup or it relaxes back to its initial spherical shape after a series of damped oscillatory deformations. Also, drop breakup mechanisms significantly differs in different mass transfer rates. Hence, based on the present results, it is found that the present method can describe the large deformations and breakup of droplets along with the accurate treatment of the surface tension and bulk solubility.

BIBLIOGRAPHY

[1] B. Jonnson, B. Lindman, K. Holmberg, and B. Kronberg, "Surfactants and polymers in aqueous solutions," *John Wiley and Sons*, 1998.

[2] U. Olgac, A. D. Kayaalp, and M. Muradoglu, "Bouyancy-driven motion and breakup of viscous drops in constricted capillaries," *International Journal of Multiphase Flow*, vol. 32, pp. 1055–1071, 2006.

[3] W. T. F. Encyclopedia., "Surfactant," *http://en.wikipedia.org/wiki/Surfactant.html*, 2006.

[4] M. Malmsten, "Surfactants and polymers in drug delivery," *Marcel Dekker*, 2002.

[5] S. V. D. Graaf, C. G. P. H. Schroen, R. G. M. V. D. Sman, and R. M. Boom, "Influence of dynamic interfacial tension on droplet formation during membrane emulsification," *Journal of Colloid and Interface Science*, vol. 277, pp. 456–463, 2004.

[6] R. J. Pugh and L. Bergstrom, "Surface and colloid chemistry in advanced seramic processing," *Marcel Dekker*, 2002.

[7] M. R. Porter, "Handarticle of surfactants," *Blackie Academic and Professional*, 1994.

[8] R. Sharma, "Surfactant adsorption and surface solubilization," *ACS Symposium Series*, 1995.

[9] H. P. Greenspan, "On the dynamics of cell cleavage," *Journal of Theoritical Biology*, vol. 65, pp. 79–99, 1976.

[10] ——, "On fluid mechanical simulation of cell division and movement," *Journal of Theoritical Biology*, vol. 70, pp. 125–134, 1977.

[11] ——, "On the deformation of a viscous droplet caused by variable surface tension," *Studies in Applied Mathematics*, vol. 57, pp. 45–58, 1977.

[12] H. A. Stone and L. G. Leal, "The effects of surfactants on drop deformation and breakup," *Journal of Fluid Mechanics*, vol. 220, pp. 161–186, 1990.

[13] J. Scholey, I. Brust-Mascher, and A. Mogilner, "Cell division," *Nature*, vol. 422, pp. 746–752, 2003.

[14] R. Rappaport, "Cytokinesis in animal cells," *Cambridge University Press*, 1996.

[15] T. Sapir and A. Nir, "A hydrodynamic study of the furrowing stage during cleavage," *Physicochemical Hydrodynamics*, vol. 6, pp. 803–814, 1985.

[16] D. Zinemanas and A. Nir, "On the viscous deformation of biological cells under anisotropic surface tension," *Journal of Fluid Mechanics*, vol. 193, pp. 217–241, 1987.

[17] X. He and M. Dembo, "Numerical simulation of oil-droplet cleavage by surfactant," *Journal of Biomechanical Engineering*, vol. 118, pp. 201–209, 1996.

[18] ——, "On the mechanics of the first cleavage division of the sea urchin egg," *Experimental Cell Research*, vol. 233, pp. 252–273, 1997.

[19] W. J. Milliken, H. A. Stone, and L. G. Leal, "The effect of surfactant on the transient motion of newtonian drops," *Physics of Fluids*, vol. 5, pp. 69–79, 1992.

[20] Y. Pawar and K. Stebe, "Marangoni effects on drop deformation in an extensional flow: The role of surfactant physical chemistry. i. insoluble surfactants," *Physics of Fluids*, vol. 8, pp. 1738–1751, 1996.

[21] C. D. Eggleton and K. Stebe, "An adsorption-desorption-controlled surfactant on a deforming droplet," *Journal of Colloid and Interface Science*, vol. 208, pp. 68–80, 1998.

[22] C. D. Eggleton, T. M. Tsai, and K. Stebe, "Tip streaming from a drop in the presence of surfactants," *Physical Review Letters*, vol. 87, p. 048302, 1998.

[23] Z. He, Z. Dagan, and C. Maldarelli, "The influence of surfactant adsorption on the motion of fluid sphere in a tube: Part 1: Uniform retardation controlled by sorption kinetics," *Journal of Fluid Mechanics*, vol. 222, p. 1, 1991.

[24] A. Borhan and C. F. Mao, "Effect of surfactants on the motion of drops through circular tubes," *Physics and Fluids*, vol. 4, pp. 2628–2640, 1992.

[25] T. M. Tsai and M. J. Miksis, "The effects of surfactant on the dynamics of bubble snap-off," *Journal of Fluid Mechanics*, vol. 337, pp. 381–410, 1997.

[26] R. Johnson and A. Borhan, "Effects of insoluble surfactants on the pressure-driven motion of a drop in a tube in the limit of high surfactant coverage," *Journal of Colloid and Interface Science*, vol. 218, pp. 184–200, 1999.

[27] ——, "Pressure-driven motion of surfactant-laden drops through cylindirical capillaries: Effect of surfactant solubility," *Journal of Colloid and Interface Science*, vol. 261, pp. 529–541, 2003.

[28] M. A. Drumright-Clarke and Y. Renardy, "The effect of insoluble surfactant at dilute concentration on drop-breakup under shear with inertia," *Physics of Fluids*, vol. 16, pp. 14–21, 2004.

[29] J. Lee and C. Pozrikidis, "Effect of surfactants on the deformation of drops and bubbles in navier-stokes flow," *Computers & Fluids*, vol. 35(1), pp. 43–60, 2006.

[30] J. J. Sun and H. K. Zhao, "An eulerian formulation for solving partial differential equations along a moving interface," *Journal of Scientific Computing*, vol. 19, pp. 573–593, 2003.

[31] J. J. Sun, Z. Li, J. Lowengrub, and H. K. Zhao, "A level-set method for interfacial flows with surfactant," *Journal of Computational Physics*, vol. 212, pp. 590–616, 2006.

[32] A. James and J. Lowengrub, "A surfactant-conserving volume-of-fluid method for interfacial flows with insoluble surfactant," *Journal of Computational Physics*, vol. 201, pp. 685–722, 2004.

[33] U. Olgac and M. Muradoglu, "Effects of soluble surfactants on the dynamics of buoyancy-driven viscous drops," *Preprint(to be submitted)*, 2006.

[34] S. O. Unverdi and G. Tryggvason, "A front tracking method for viscous incompressible multiphase flows," *Journal of Computational Physics*, vol. 100, pp. 25–37, 1992.

[35] H. A. Stone, "A simple derivation of the time dependent convection diffusion equation for surfactant transport along a deforming interface," *Physics of Fluids A*, vol. 2, pp. 111–112, 1990.

[36] C. Peskin, "Numerical analysis of blood flow in the heart," *Journal of Computational Physics*, vol. 25, pp. 220–252, 1977.

[37] F. H. Harlow and E. Welch, "Numerical calculation of time-dependent viscous incompressible flow of fluids with free surface," *Physics of Fluids*, vol. 8, pp. 2182–2189, 1965.

[38] G. Tryggvason, B. Bunner, A. Esmaeeli, D. Juric, N. Al-Rawahi, W. Tauber, J. Han, S. Nas, and Y. J. Jan, "A front tracking method for the computations of multiphase flows," *Journal of Computational Physics*, vol. 169, pp. 708–739, 2001.

[39] J. C. Adams and Mudpack, "Multigrid fortran software for the efficient solution linear elliptical partial differential equations," *Journal of Applied Mathematics and Computations*, vol. 34, p. 113, 1989.

[40] S. Osher and J. A. Sethian, "Fronts propogating with curvature-dependent speed: Algorithms based on hamilton-jacobi formutions." *Journal of Computational Physics*, vol. 79, pp. 12–49, 1988.

[41] M. Sussman, P. Smereka, and S. Osher, "A level set approach for computing solutions to incompressible two-phase flow." *Journal of Computational Physics*, vol. 114, pp. 146–159, 1994.

[42] J. Zhang, D. M. Eckmann, and P. Ayyaswamy, "A front tracking method for a deformable intravascular bubble in a tube with soluble surfactant transport." *Journal of Computational Physics*, vol. 214, pp. 366–396, 2006.

VITA

Emrah Gölbaşı was born in Antalya, Turkey on December 15, 1980 . He graduated from Izmir Science High School in 1999. He received the B. Sc. degree in Mechanical Engineering from Istanbul Technical University (ITU), in 2004. In October 2004, he joined to the Mechanical Engineering Department of Koç University, Istanbul, Turkey as a teaching and research assistant.